Faculty and Researchers | Faculty and Researchers' Publications

2016

# Evolution of a Canada Basin iceocean boundary layer and mixed layer across a developing thermodynamically forced marginal ice zone

Gallaher, Shawn G.; Stanton, Timothy P.; Shaw, William J.; Cole, Sylvia T.; Toole, John M.; Wilkinson, Jeremy P.; Maksym, Ted; Hwang, Byongjun

AGU

**RESEARCH ARTICLE**

**Correspondence to:**
S. Gallaher,
sggallah1@nps.edu

# Evolution of a Canada Basin ice-ocean boundary layer and mixed layer across a developing thermodynamically forced marginal ice zone

**Shawn G. Gallaher[1], Timothy P. Stanton[1], William J. Shaw[1], Sylvia T. Cole[2], John M. Toole[2], Jeremy P. Wilkinson[3], Ted Maksym[2], and Byongjun Hwang[4]**

[1]Naval Postgraduate School, Monterey, California, USA, [2]Woods Hole Oceanographic Institution, Woods Hole, Massachusetts, USA, [3]British Antarctic Survey, Cambridge, UK, [4]Scottish Association of Marine Science, Oban, UK

**Abstract** A comprehensive set of autonomous, ice-ocean measurements were collected across the Canada Basin to study the summer evolution of the ice-ocean boundary layer (IOBL) and ocean mixed layer (OML). Evaluation of local heat and freshwater balances and associated turbulent forcing reveals that melt ponds (MPs) strongly influence the summer IOBL-OML evolution. Areal expansion of MPs in mid-June start the upper ocean evolution resulting in significant increases to ocean absorbed radiative flux (19 W m$^{-2}$ in this study). Buoyancy provided by MP drainage shoals and freshens the IOBL resulting in a 39 MJ m$^{-2}$ increase in heat storage in just 19 days (52% of the summer total). Following MP drainage, a near-surface fresh layer deepens through shear-forced mixing to form the summer mixed layer (sML). In late summer, basal melt increases due to stronger turbulent mixing in the thin sML and the expansion of open water areas due in part to wind-forced divergence of the sea ice. Thermal heterogeneities in the marginal ice zone (MIZ) upper ocean led to large ocean-to-ice heat fluxes (100–200 W m$^{-2}$) and enhanced basal ice melt (3–6 cm d$^{-1}$), well away from the ice edge. Calculation of the upper ocean heat budget shows that local radiative heat input accounted for at least 89% of the observed latent heat losses and heat storage (partitioned 0.77/0.23). These results suggest that the extensive area of deteriorating sea ice observed away from the ice edge during the 2014 season, termed the "thermodynamically forced MIZ," was driven primarily by local shortwave radiative forcing.

## 1. Introduction

### 1.1. Seasonal Ice Loss in the Western Arctic

The Western Arctic seasonal ice zone is expanding. The seasonal ice zone (SIZ) is defined as the region between maximum sea ice extent in late spring and minimum sea ice extent in late summer. The largest growth of this region is occurring in the Beaufort Sea and Canada Basin where the SIZ area has increased by 5.2% and 3.6% per decade between 1968 and 2008 [*Tivy et al.*, 2011]. The lower areal extent of sea ice during summer has led to a 2–4% per year increase in radiative input to the ocean mixed layer between 1979 and 2005 [*Perovich et al.*, 2007a]. Identifying the processes that drive SIZ expansion requires an understanding of how this incoming solar radiation is absorbed and redistributed within the ice-ocean system. In this study, summer observations from the 2014 Office of Naval Research Marginal Ice Zone experiment in the Canada Basin are used to investigate the evolution of the turbulent ice-ocean boundary layer and mixed layer, and consequent effects on the partitioning of absorbed radiation in the upper ocean.

### 1.2. The Summer Seasonal Ice Zone in the Canada Basin

Large vertical fluxes of heat and freshwater occur in the SIZ ice-ocean system during the spring-summer transition from full ice cover to open water. In the Canada Basin, defined as the area in Figure 1a enclosed by the 3000 m isobath [*Lane*, 1997], fundamental changes to the thermodynamics of this system start near the summer solstice as sunlight enters the ocean through thin ice and leads. When melt ponds are present, radiative fluxes through thick sea ice can be significant as well [*Light et al.*, 2008]. In addition to facilitating upper ocean heating, melt pond drainage is a significant source of freshwater to the upper ocean. Melt pond water drains to the upper ocean through leads, cracks, enlarged brine channels [*Polashenski et al.*, 2012], or by percolation through the sea ice [*Eicken et al.*, 2002]. Freshwater from Mackenzie River runoff has
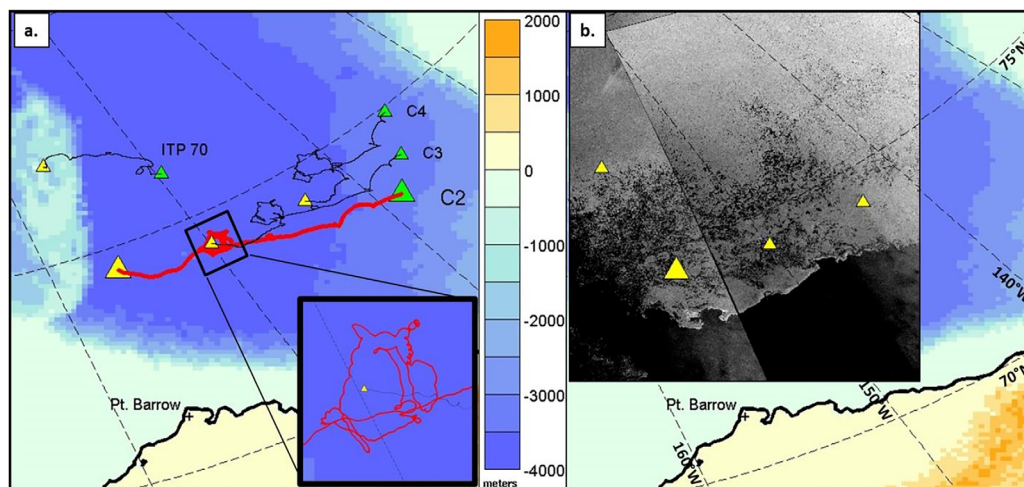
**Figure 1.** (a) Topo-bathymetric map background of the Canada Basin showing the time series start positions (green triangles) of ITP-V 70 and MIZ clusters 2–4 on 30 May (YD 150), and end positions (yellow triangles) on 19 August (YD 231), with the exception of ITP-V 70 which terminated on 15 July (YD 196). C2 is the primary focus of this study (red track). (b) Merged RadarSat-2 images from 19 and 21 August (YDs 231 and 233), light/white areas represent ice covered portions of the ocean.

also been shown to reach the Southern Canada Basin under certain conditions [*Macdonald et al.*, 1999]; however, significant contributions of heat and freshwater are generally confined further southeast to the Beaufort Sea/Shelf [*Nghiem et al.*, 2014].

As summer progresses, radiative input to the ocean increases in response to larger open water areas. Basal ice melt accelerates during this period, adding further to the freshwater storage of the upper ocean. The combined inputs of melt pond drainage and basal ice melt can lead to surface fresh layers. Shallow fresh (2–4 psu) layers were observed in leads by *Paulson and Pegau* [2001] during the Surface Heat Budget of the Arctic Ocean (SHEBA) experiment with depths that extended to 1.2 m and temperatures as high as +1.6°C. These findings were confirmed by Autonomous Underwater Vehicle (AUV) observations, which showed surface trapped meltwater layers developed during low stress conditions and extended beyond the lead when ice drafts were less than the depth of the surface fresh layers [*Hayes and Morison*, 2008].

Ultimately, the SIZ transitions into a marginal ice zone (MIZ) environment. There is no clear definition of the MIZ [*Lee et al.*, 2012]. *Wadhams* [2000] refers to the MIZ as a buffer between open water and the ice pack (ice concentration >70%) where open water processes affect the sea ice cover. These large spatial variations in sea ice coverage and composition generate correspondingly large spatial gradients in upper ocean properties.

### 1.3. The Ice-Ocean Boundary Layer and Heat Redistribution

The redistribution of radiative energy absorbed in the upper ocean depends largely on the vertical extent of the turbulent ice-ocean boundary layer. The ice-ocean boundary layer (IOBL) is the actively mixing portion of the ocean mixed layer (OML) where turbulent eddies, generated by shear between wind-forced ice motion and the upper ocean, efficiently transport momentum, heat, and salt [*McPhee*, 2008]. During winter, the IOBL is neutrally to unstably stratified allowing strong wind events to deepen the IOBL beyond the previously established winter mixed layer (wML) depth. This deepening can result in IOBL warming as heat trapped within the winter pycnocline stratification is entrained upward [*Jackson et al.*, 2012]. In spring, IOBL heating is augmented by radiative input absorbed directly into the upper few meters of the ocean. The amount of basal ice melt generated from these IOBL heat gains is dependent on the magnitude of turbulent heat flux, which is driven by turbulent shear velocity ($u_*$) and the water temperature above freezing ($\delta T$) [*McPhee*, 1992].

In summer, upper ocean stratification increases and the IOBL shoals as turbulent eddies expend kinetic energy to erode near-surface stratification, limiting the penetration of turbulent mixing. Boundary layer model results show that the IOBL depth can contract to <10 m during summer in response to basal ice melt [*Toole et al.*, 2010; *Vivier et al.*, 2016]; however, the effects of melt pond drainage on the IOBL have

been largely unexplored. Ultimately, the fresh melt layer develops into the summer mixed layer (sML) resulting in the dynamic decoupling of the underlying wML.

Observations from 2004 to 2009 show that freshening within the Canada Basin has led to stronger stratification and shallower mixing/mixed layers, with average sML and wML depths of 16 and 24 m, respectively [*Toole et al.*, 2010]. Thinning of the IOBL permits greater heat storage within the residual wML, as that layer is able to directly absorb incoming radiation without turbulent vertical mixing. This forms a near-surface temperature maximum (NSTM) in the stratified water just below the sML [*Jackson et al.*, 2010]. Heat storage observed in the Canada Basin between 1993 and 2009 has increased by 0.5°C in the wML and by 1.5°C in the NSTM [*Jackson et al.*, 2011]. An increase in the heat just beneath the Canadian Basin wML, associated with the intrusion of Pacific Summer Water, was also observed between 2003 and 2013 [*Timmermans et al.*, 2014]; however, this heat source is effectively isolated from the ice-ocean interface due to strong stratification below the wML which limits entrainment to a <5 m mixing zone [*Shaw et al.*, 2009]. Thus, solar radiation is the primary source of heat to the OML in the Canada Basin SIZ during summer and is predominantly distributed between latent heat losses and mixed layer heat storage gains (sink terms). The relative radiative input to these two sinks is dependent on the characteristics of the IOBL.

In the MIZ environment, the high spatial variability of ice/water fractions lead to extreme radiative and turbulent fluxes in and out of the IOBL-OML system. Substantial ocean-to-ice heat fluxes and basal ice melt can result when winds accelerate sea ice over adjacent open water areas. In the Eastern Arctic MIZ, *McPhee et al.* [1987] found that turbulent heat flux can be as high as 200 W m$^{-2}$. During that same experiment, *Morison et al.* [1987] found that large increases in stratification, caused by high basal ice melt, can inhibit turbulent heat and momentum transfer with the ice-ocean interface. These two observations demonstrate the intricate interplay between momentum, heat, and buoyancy in a MIZ environment and the potential for highly variable melt rates.

### 1.4. Objectives

Previous large-scale studies of ice-ocean interactions in a MIZ have been focused on areas with significant ocean wave forcing in the Eastern Arctic or the Bering Sea [*MIZEX Group*, 1986], before the widespread summer ice retreat started to occur in the Canada Basin during the past decade [*Perovich et al.*, 2012]. Although the Canada Basin MIZ can be mechanically forced by summer cyclones [*Zhang et al.*, 2013], the 2014 summer wind forcing was low (study site mean ∼4 m s$^{-1}$) and close to the climatological mean (∼3.7 m s$^{-1}$, *Stegall and Zhang* [2012]). Furthermore, the Canada Basin MIZ exists in an enclosed basin not subject to long period swell until late in the ice retreat [*Thomson and Rogers*, 2014]. These characteristics suggest thermodynamics are an important part of the late summer condition in this region.

In this study, we use data from the Office of Naval Research MIZ program to explore upper ocean thermodynamics as ice-deployed autonomous sensors drift on ice floes melting and mechanically deteriorating over the course of the summer season. Our specific objectives are to: (1) provide a high resolution overview of the IOBL-OML system as it changes during the summer; (2) identify unique regimes when OML heat storage and/or latent heat losses are enhanced by IOBL processes; (3) determine the processes that lead to sML and NSTM development; and (4) explore processes leading to the large area of deteriorating sea ice observed away from the sea ice edge during the 2014 summer (Figure 1b). Investigation of these objectives will provide a better understanding of the ice-ocean system beneath the Western Arctic SIZ and determine the specific air-ice-ocean interactions contributing to increased seasonal melt in the Canada Basin.

## 2. Air-Ice-Ocean Observations

### 2.1. Marginal Ice Zone Experiment

To gain a better understanding of the expanding Western Arctic SIZ and associated MIZ, the MIZ field program collected a wide-range of in situ and satellite-based observations during the spring and summer of 2014 in the Canada Basin. Four multisensor clusters were deployed ∼100 km apart along the 135°W meridian. These clusters were programmed to observe air-ice-ocean conditions throughout the SIZ transition from compact ice cover in spring to a fully developed MIZ in late summer. Each cluster contained a tightly grouped set of autonomous platforms to measure atmospheric conditions, surface solar radiation, ice thickness and temperature, ocean hydrographic profiles, and ice-ocean turbulent fluxes. In situ observations

were complemented by remote sensing products, which were used to determine ice conditions on large spatial scales. For a full description of the MIZ experiment, see *Lee et al.* [2012] and https://www.apl.washington.edu/project/project.php?id=miz.

## 2.2. Data Sources

Observations of near-interface turbulent processes were obtained from the Naval Postgraduate School Autonomous Ocean Flux Buoy 33 (AOFB 33) located at MIZ cluster 2 (C2) (AOFB website https://www.oc.nps.edu/~stanton/fluxbuoy). The primary AOFB sensor was the custom-built ocean flux package, consisting of (with accuracies) a 4-path, three-dimensional acoustic travel-time current meter (ACM) ($\pm 0.25$ mm s$^{-1}$ RMS noise level), a free-flushing inductive conductivity cell ($\pm 0.002$ mS cm$^{-1}$), and a fast low-noise thermistor ($\pm$ 1 mC). These sensors were integrated to form a 0.001 m$^{-3}$ sample volume located initially at ~2.5 m below the ice-ocean interface (~4.5 m depth). Data were reported at 2 Hz and allowed the direct estimation of oceanic vertical turbulent fluxes of momentum, heat, and salt using eddy correlation methods. The MIZ program sampling strategy typically enabled the instruments to run for 35 min every 2 h. At 2 m above the sea ice surface, wind velocity (Vaisala Multiweather Sensor) and incident shortwave solar irradiance (Hukseflux SR03) were collected every 15 min. The pyranometer measured incident solar irradiance over a spectral range between 280 and 3000 nm.

Observations of upper ocean salinity and temperature were provided by the Ice-Tethered Profiler [*Krishfield et al.*, 2008; *Toole et al.*, 2011]. The Ice-Tethered Profiler was also equipped with a velocity sensor (ITP-V) to measure ocean velocities and upper ocean turbulence [*Cole et al.*, 2014]. Data from ITP-V 77 was used extensively in this study and colocated on the same ice floe with AOFB 33 at C2. The ITP-V provided profiles of in situ temperature, salinity, and velocity every 0.25 m, which were binned to 1 m, using a CTD profiler package crawling along a weighted wire connected to a surface buoy. The ITP-V profiled between 7 and 250 m every 3 h. In addition, at roughly 6 h intervals, time series data were collected at a fixed depth of 6.5 m (initially ~4.5 m below the ice-ocean interface) for 20 min periods from which turbulent fluxes of heat, salt, and momentum were estimated using eddy correlation methods. A full description of velocity data processing is provided in *Cole et al.* [2015]. In addition, at 6 m depth, a fixed SeaBird SBE-37 MicroCAT sensor sampled salinity and temperature every 15 min [*Krishfield et al.*, 2008].

Ice Mass Balance (IMB) instruments were deployed to measure sea ice temperature and thickness. Two different IMB systems were used: (1) the Scottish Association for Marine Science (SAMS) IMB 17 [see *Jackson et al.*, 2013] and (2) the Cold Regions Research and Engineering Laboratory (CRREL) IMB 2014C [see *Polashenski et al.*, 2011]. These IMBs were deployed at the center of C2 on ~1.8 m thick sea ice with ~0.25 m thick snow cover. In this study, an average of the SAMS and CRREL IMB bottom interface observations were used to represent C2 ice base changes. All other sea ice observations are from the SAMS IMB. Figure 2 shows the relative vertical positions of the AOFB, ITP-V, and IMB sensors.

In addition to these in situ observations, several satellite resources were exploited to characterize surface sea ice conditions. Two SAR products, provided by the Center for Southeastern Tropical Advanced Remote Sensing (CSTARS), were used in this study: (1) TerraSAR-X images at 8.3 m pixel spacing used to calculate local area open water fractions about MIZ C2 and (2) RadarSat-2 images at 100 m pixel spacing to provide general regional area ice conditions. Declassified visible gray scale satellite images at 1 m resolution were also used to characterize the local surface sea ice conditions and estimate melt pond coverage.

Webcam images, wind estimates, and pyranometer data complete the data set. Webcam images were taken every 6 h from wave buoy (WB) 211 stationed ~25 m from AOFB 33 and ITP-V 77 to show surface conditions in C2's immediate vicinity. Failure of the AOFB 33 wind sensor between year day (YD) 198 and YD 231 required use of the RM Young anemometer mounted ~2 m above the sea ice surface on Automated Weather Station 2 (AWS 2). Additionally, hourly pyranometer observations from AWS 3 (C3) were linearly interpolated into the AOFB 33 shortwave radiation flux time series between YDs 196.8 and 201.8 due to a temporary power outage. Data from the Climate Forecast System Reanalysis (CFSR) were used to provide 10 m winds at ITP-V 70 for air-water stress calculations. CFSR is a fully coupled modeling system assimilating in situ and satellite derived air, ice, and ocean observations into a 0.313 degree reanalysis model (for full description, see *Saha et al.* [2010]).
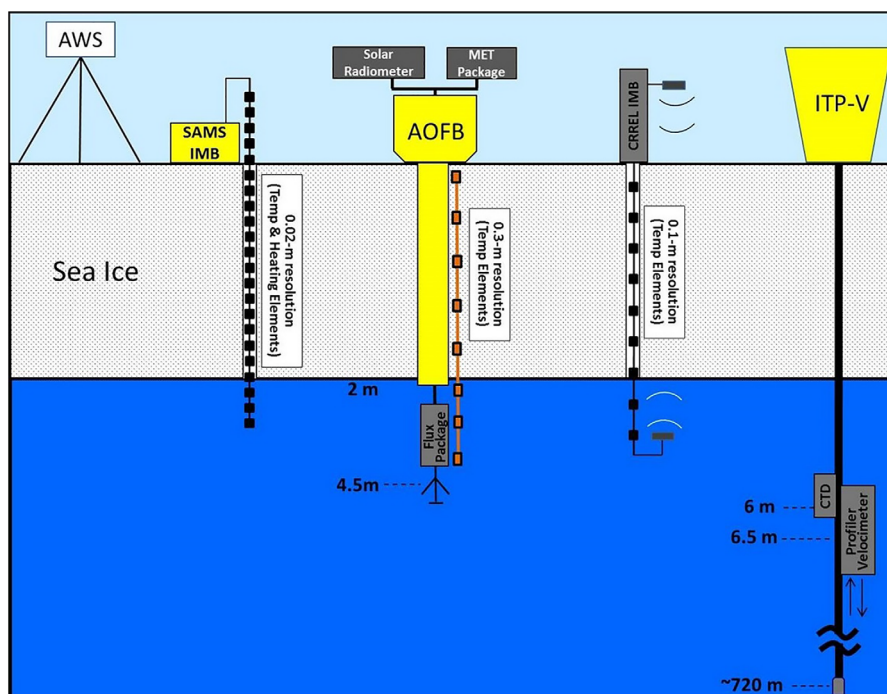
**Figure 2.** Schematic diagram showing relative vertical positions of instruments deployed on the MIZ C2 ice floe.

In combination, the AOFB, ITP-V, IMBs, and satellite imagery provide key information for understanding air-ice-ocean interactions during the MIZ field program. This includes sea ice conditions on multiple spatial scales, surface radiative fluxes, ocean turbulent fluxes at 4.5 and 6.5 m, and ocean temperature, salinity, and velocity between 4.5 and 250 m at 1 m resolution. These combined data sets were captured during an ice floe drift track through the Canada Basin SIZ and provide the most complete geophysical representation of the temporal evolution of the IOBL and OML under a developing MIZ ever observed by autonomous means.

The focus of the present study is the period 30 May to 19 August 2014 (YDs 150–231). Instruments at MIZ clusters 2–4 (C2–C4) returned data throughout this period as they traversed the Canada Basin (Figure 1a). ITP-V 70, a prototype MIZ asset deployed 1 year earlier, exhausted the battery on its underwater sensor on YD 196. C2 returned the most complete data set, and is thus the focal point of this work. Data from C3, C4, and ITP-V 70 are used for regional comparisons. Data from C1 was not used in this study since no ITP-V or AOFB was deployed at this site. C5 was not used because it was not deployed until late summer. Observations from the ice-deployed instruments included both temporal and spatial variability of upper ocean properties; the primary attention here is on the temporal evolution.

## 3. Methods

### 3.1. Turbulent Mixing Layer and Summer Season Mixed Layers
High resolution salinity and velocity data of the upper ocean provided a means of tracking the maximum vertical extent of shear generated turbulence identifying the IOBL. We estimated the IOBL using the bulk Richardson number [e.g., *Large et al.*, 1994]

$$Ri_{bulk} = \frac{g(\Delta\rho)}{\rho_o[(\Delta u)^2 + (\Delta v)^2]}\Delta z, \qquad (1)$$

where $\Delta\rho$, $\Delta u$, and $\Delta v$ are the changes in density and horizontal velocity across water thickness $\Delta z$, $g$ is the gravitational acceleration (9.81 m s$^{-2}$), and $\rho_o$ is the reference density (1023 kg m$^{-3}$). $\Delta u$ and $\Delta v$ were calculated by taking the difference of AOFB/ITP-V velocities relative to the ice velocity, assuming that the upper
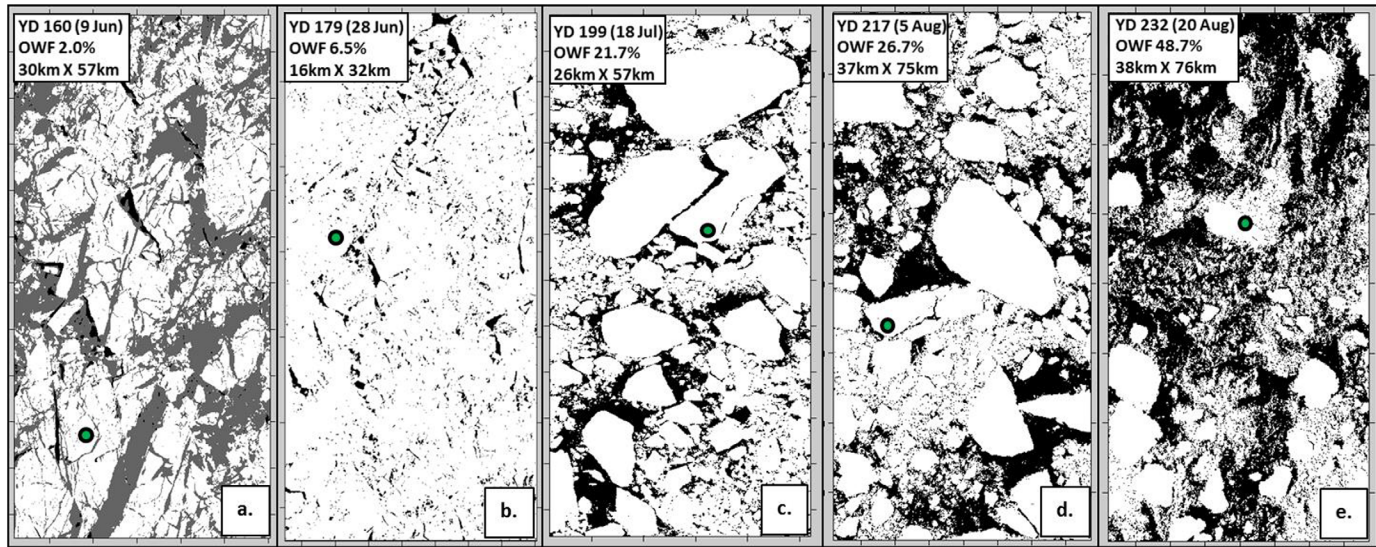
**Figure 3.** (a–e) 5 of the 21 TerraSAR-X satellite images used to estimate open water fraction ($A_{OWF}$) for the ocean radiative flux calculation. The location of the MIZ cluster 2 (C2) instrument array is represented by the green circle. These images document the progression of the MIZ C2 locale from compact sea ice in late spring (a) toward a marginal ice zone condition with large open water areas at the end of summer (e).

level of the slab motion in the bulk Richardson number calculation was the ice velocity. When $Ri_{bulk}$ exceeded a critical value ($Ri_c$), IOBL deepening was assumed to terminate as the mixed layer shear becomes insufficient to overcome upper ocean density jumps (pycnoclines). The critical value for $Ri_{bulk}$ is not well defined; however, a numerical model study conducted by *Price et al.* [1986] showed $Ri_c = 0.65$ effectively diagnosed the depth of the ocean mixed layer. Thus, the IOBL for this study is considered all depths shallower than $Ri_{bulk} = 0.65$.

The wML and sML were used as control volumes for the local heat and freshwater budgets, therefore, clear definitions of each of these features were required. The wML resided above a deep ($\sim$35–45 m) winter pycnocline defined for this study by the 1023.5 kg m$^{-3}$ isopycnal. This material surface was selected because it tracked the upper portion of the winter pycnocline throughout the time series. For the pycnocline at the base of the sML, we used the terminology and method of *Jackson et al.* [2010], which defines the summer halocline by the maximum water column buoyancy frequency

$$N^2_{max} = -\frac{g}{\rho_o}\frac{d\rho}{dz}_{max},\tag{2}$$

where $d\rho/dz$ is the potential density gradient. However, because density gradients at the base of the sML during initial development were weak, we modified the definition from the water column $N^2$ maximum to the $N^2$ maximum above the deep winter pycnocline following development of the NSTM. The NSTM is defined by the following criteria: (1) a near-surface temperature maximum that is at least 0.1°C above a deeper temperature minimum, (2) a salinity lower than 31 psu, and (3) at least a 0.2°C temperature above freezing [*Jackson et al.*, 2010]. The wML, sML, and NSTM are overlaid in Figure 8c and show their relative vertical extent.

### 3.2. Open Water Fraction and Melt Pond Coverage

TerraSAR-X images collected over C2 were used to estimate the areal fraction of open water ($A_{OWF}$). For each image, a combination of median, Gaussian, and bilateral filters [*Tomasi and Manduchi*, 1998] were applied to reduce speckle noise in the raw Synthetic Aperture Radar (SAR) images, and $A_{OWF}$ was calculated using a parametric kernel graph cuts algorithm [*Salah et al.*, 2011]. Twenty-five images were processed for the focus period, five of which are presented in Figure 3. Four images between YDs 217 and 226 were excluded due to large variability in derived $A_{OWF}$. Comparisons to 1 m visible imagery suggest that ice area may have been over represented in the lower resolution SAR imagery when extensive areas of small ice
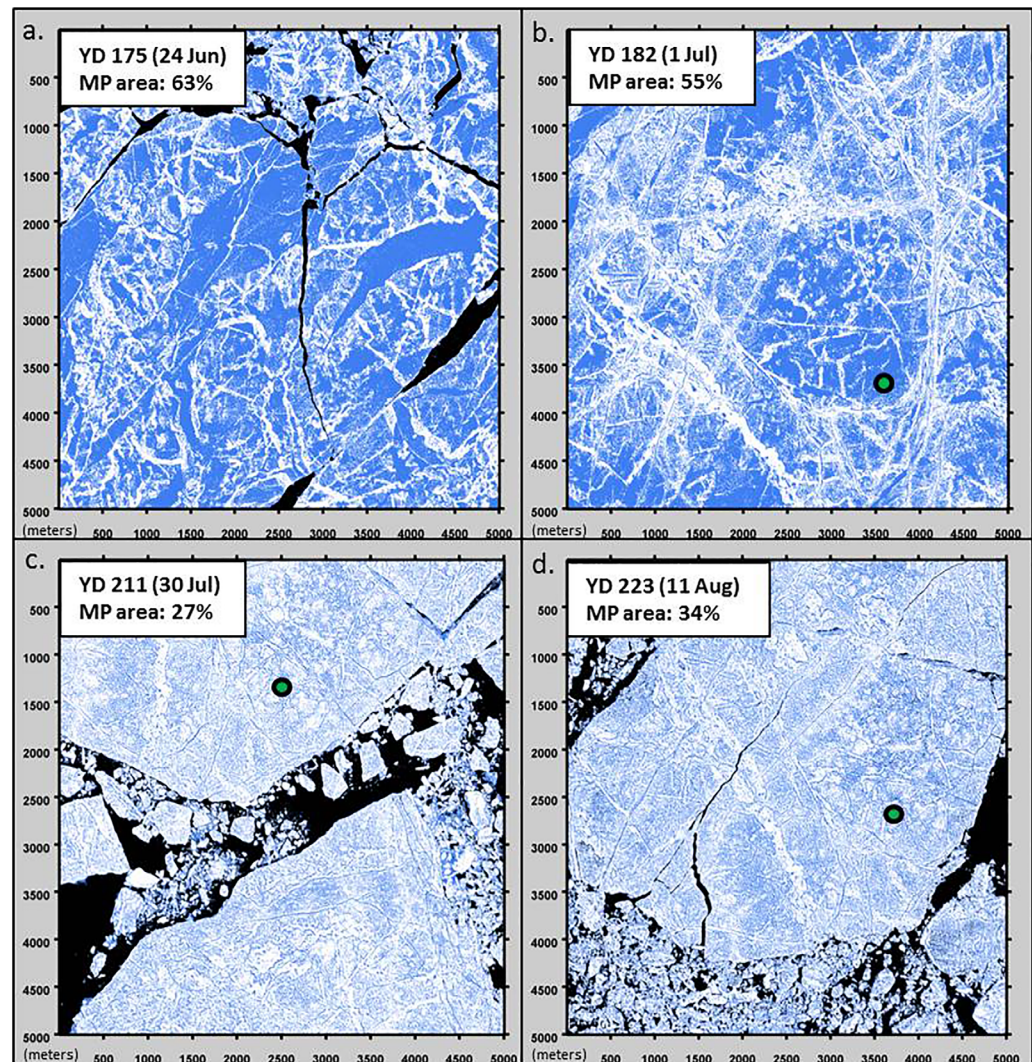
**Figure 4.** (a–d) False color visible satellite images (1 m res.) showing the evolution of melt pond coverage (light blue) at MIZ C2 (green dots) and were used to estimate the through-ice component of solar radiative flux to the ocean.

floes and brash were present. Estimates of $A_{OWF}$ from the remaining 21 images were linearly interpolated between observations across the SAR image time series (YD 150–232).

The areal coverage of melt ponds ($A_{MP}$) on ice floes was approximated using high resolution (1 m) visible satellite imagery. Since open water, melt ponds, and sea ice had large differences in visible wavelength albedo, a histogram of gray scale pixel intensities generally produced tri-modal distributions. Thresholds can be applied in the valleys of these three peaks to designate pixel cells into one of the three categories [*Kim et al.*, 2013]. Four 25 km$^2$ images were selected based on image availability, proximity to C2, and cloud contamination (Figure 4). The image taken on YD 175 (Figure 4a) was the only image not acquired directly over C2 (~35 km north), but was the only image available near the time of maximum melt pond coverage. Estimates of $A_{MP}$ were linearly interpolated between observations across the visible image time series (YD 149–223). $A_{MP}$ is assumed constant between YDs 223 and 231 due to the lack of visible imagery after YD 223.

### 3.3. Mixed Layer Heat and Freshwater Budgets

A simple 1-D heat budget was calculated, at ~3 h intervals, to determine how ocean absorbed solar radiation (source term) was distributed between OML heat storage (sink term 1) and latent heat losses (sink term 2). Radiative input into the ocean was not directly observed during this study, thus, a combination of air-

side shortwave radiation observations, satellite imagery, and published parameterizations were used to estimate solar radiation entering the upper ocean. Ocean radiative fluxes have an open-water and under-ice component. The open-water component was estimated by [e.g., *Stanton et al.*, 2012]

$$F_{rad-owf} = F_{rad} A_{OWF} (1 - \alpha_{ocn}),$$  (3)

where $F_{rad}$ is the observed downwelling irradiance from the AOFB, $A_{OWF}$ is the fraction of open water derived from SAR imagery, and $\alpha_{ocn}$ is the albedo of open water (0.066) [*Pegau and Paulson*, 2001].

To calculate the under-ice component of ocean radiative flux, we used the *Light et al.* [2008] sea ice shortwave downwelling flux equation scaled by the ice cover fraction $(1 - A_{OWF})$ and the optical properties of the sea ice surface conditions to form:

$$F(z_{ice})_{rad-underice} = F_{rad}(1 - A_{OWF})[A_{ice}(1 - \alpha_{ice})I_{ice} + A_{MP}(1 - \alpha_{MP})I_{MP}].$$  (4)

$A_{ice}$ is the fraction of total ice coverage that is unponded $(1 - A_{MP})$ and $A_{MP}$ is the fraction of total ice coverage that is ponded derived from visible satellite imagery. The $\alpha_{ice}$ and $\alpha_{MP}$ terms are the albedos, and the $I_{ice}$ and $I_{MP}$ terms are the attenuation equations $(I = I_o \exp(-Kz_{ice}))$ for melting and ponded multiyear ice (predominate ice type at C2). For this study, the applicable Table 4 values from *Light et al.* [2008] were used to estimate albedo $(\alpha)$, surface transmission parameter $(I_o)$, and extinction coefficient (K). Local sea ice thickness $(z_{ice})$ was derived from IMB observations. $\alpha$, I, and K also have distinct values for the visible and near-infrared portions of the incoming solar energy. The pyranometer sampled both the visible and near-infrared spectra together. Hence, the solar data were partitioned as 0.7 (visible) and 0.3 (near-infrared), consistent with the approximately two-thirds to three-quarters of solar energy being in the visible range [*Perovich and Polashenski*, 2012]. Of note, $F_{rad-underice}$ was set to zero when dry snow was suspected to cover the sea ice (YDs 150–156).

The sum of equations (3) and (4) provides the radiative source term for the heat balance calculation and is referred to as the total ocean radiative flux ($F_{rad-ocn}$), or integrated in time, the total ocean radiative energy ($Q_{rad-ocn}$). The sea ice characterization afforded by the MIZ space-based assets was remarkable and resulted in a robust $F_{rad-ocn}$ estimate. This method requires that we assume the $A_{OWF}$ and $A_{MP}$ determined at the larger spatial scales, 45 and 5 km square, respectively, were representative of the radiative influence near C2. The authors acknowledge that this local scale may not always be appropriate for all conditions; however, comparisons of $A_{OWF}$ to smaller area TerraSAR-X and 1 m visible satellite imagery show similar $A_{OWF}$ results down to ~10 km square (not shown).

For the first sink term, OML heat storage per m$^2$ was calculated from the amalgamated fixed-depth AOFB and MicroCAT CTD, and profiled ITP data by

$$Q_{oml} = c_p \rho_o \int_{z_2}^{z_1} \delta T(s,p) dz,$$  (5)

where $c_p$ is the specific heat capacity of sea water (~3986 J kg$^{-1}$ C$^{-1}$), and $\delta$T is the in situ temperature above freezing (T − T$_f$). Given that T$_f$ changes with salinity, a reference salinity (S$_{ref}$) of 28.7 psu was assumed and yields a freezing temperature of ~−1.57°C [*UNESCO*, 1983]. S$_{ref}$ is the approximate average salinity along the 1023.5 kg m$^{-3}$ isopycnal (winter pycnocline). Use of a reference freezing temperature allowed for a heat as opposed to a temperature budget. Comparison of the heat storage results between local and referenced freezing temperatures yielded a difference of ~6 MJ m$^{-2}$ over the study period. All salinity and temperature data from the AOFB and ITP profiler were calibrated to the MicroCAT CTD. Just 31 of 639 profiles were missing from the ITP-V profiling CTD, thus data were linearly interpolated across all time gaps. The upper level of integration (z$_1$) is the shallowest observed temperature and salinity depth (4.5 m) and the lower limit (z$_2$) is the material surface defined by the winter pycnocline. After the sML forms around YD 192, z$_2$ becomes the base of the sML identified by the summer halocline depth. For evaluation of the wML during this period, the base of sML becomes z$_1$ and the winter pycnocline becomes z$_2$. The OML is defined as the entire ocean volume down to the winter pycnocline. The OML before YD 192 is equal to the wML; however, the OML after YD 192 is the combined sML and wML.

For the second sink term, latent heat losses per m$^2$ from the IMB data were calculated by

$$Q_{lh} = q_{lh} \rho_{ice} \Delta z_{ice}, \tag{6}$$

where $q_{lh}$ is the latent heat of fusion for sea ice ($3 \times 10^5$ J kg$^{-1}$), $\rho_{ice}$ is the density of sea ice (910 kg m$^{-3}$), and $\Delta z_{ice}$ is the change in the bottom sea ice interface in m$^3$/m$^2$.

The flux form of the sink terms are presented in the results and were determined by dividing equations (5) and (6) by the analysis time interval ($\Delta t = \sim 3$ h). Also, we assume upper ocean heat changes due to the long-wave radiation balance, air-water latent heat exchange, and air-water sensible heat exchange are small due to the high areal fraction of sea ice and near equal air-water temperatures observed during the study [*Persson et al.*, 2002].

Similar to the heat budget, a 1-D freshwater budget was calculated comparing sea ice melt (source) to OML freshwater storage (sink). The freshwater source term (FWC$_{ice}$) was determined from the combined observed surface and basal sea ice melt calculated by ($\rho_{ice}/\rho_{fw}$)$\Delta z_{ice}$, where $\rho_{fw}$ is the density of freshwater (1000 kg m$^{-3}$). For snow melt, $\rho_{ice}$ is replaced by $\rho_{snow}$ (360 kg m$^{-3}$).

To calculate OML freshwater storage per m$^2$, we used the *Proshutinsky et al.* [2009] freshwater content equation

$$FWC_{oml} = \int_{z_2}^{z_1} \frac{[S_{ref} - S(z)]}{S_{ref}} dz, \tag{7}$$

where $S_{ref}$ is the reference salinity (28.7 psu), and $S(z)$ is the salinity at water depth z. To partition FWC$_{oml}$ into sML and wML components, we use the same upper and lower integration limits as in equation (5). The flux form of the freshwater source and sink terms will also be presented in section 4.

In summary, this simple 1-D approach tests the local budgets in order to identify trends in ocean heating and freshening during the summer evolution. We then attempt to associate these trends with changes in the IOBL, wML, sML, and/or the sea ice. Significant residuals of heat and freshwater will be assumed due to radiative flux estimate errors, lateral advection, or potentially vertical diffusion from below the OML material surface.

### 3.4. Turbulent Exchange of Heat, Salt, and Momentum

To identify active and inactive periods of mixing, heat exchange, and salt exchange with the ice-ocean interface, turbulent fluxes of momentum, heat, and salt were calculated from the fixed-depth flux packages using eddy correlation methods. Spectral covariance estimates of perturbation pairs were determined across a selected frequency range to avoid contamination from surface gravity waves, package vibration, and potentially internal gravity waves. For the AOFB, a cross spectral analysis was performed on each 35 min sample. Flux estimates ($<w'x'>$) were calculated by summing the covariance in the spectral bins spanning the outer scale turbulent eddy frequencies by [*Shaw and Trowbridge*, 2001]

$$\langle w'x' \rangle \Big|_{f_1}^{f_2} = \int_{f_1}^{f_2} Co_{wx}(f) df, \tag{8}$$

where $Co$ is the cospectrum, $w$ is the vertical velocity perturbation, $x$ is the vector ($u$, $v$) or scalar ($T$, $S$) perturbation variables, and $f_1$ and $f_2$ are the low- and high-frequency limits of the energy-containing range (0.0029–0.12 Hz in this study). For the ITP-V, fluxes were calculated by averaging covariance results over each 20 min sample, after each variable was detrended and low-pass filtered at 4 s.

Turbulent fluxes of heat and salt in the vertical were then given by

$$F_H = c_p \rho_o \langle w'T' \rangle, \tag{9}$$

$$F_s = \langle w'S' \rangle, \tag{10}$$

where $<w'T'>$ and $<w'S'>$ are the kinematic heat and salt fluxes from equation (8), respectively. Freshwater flux at 4.5 m was derived from $<w'S'>_{(4.5m)}$ observations and was calculated using a modified form of equation (7) and the local salinity for $S_{ref}$. The magnitude of the turbulent momentum flux was represented by the friction velocity [e.g., *McPhee*, 2008]

**Table 1.** Acronyms and Mathematical Symbols

| Acronyms | | | Math symbols | |
| --- | --- | --- | --- | --- |
| aML | Active mixing layer | | $A_{MP}$ | Fraction of ice covered by melt ponds |
| AOFB | Autonomous Ocean Flux Buoy | | $A_{OWF}$ | Open water fraction |
| AWS | Automated Weather Station | | $\alpha$ | Albedo |
| C2/3/4 | Instrument cluster 2/3/4 | | $C_d$ | Drag coefficient |
| CFSR | Climate Forecast System Reanalysis | | $\delta T$ | Departure from freezing |
| IMB | Ice Mass Balance instrument | | $F_H$ | Ocean turbulent heat flux |
| IOBL | Ice-ocean boundary layer | | $F_{rad}$ | Incident solar radiative heat flux |
| ITP-V | Ice-Tethered Profiler—velocity | | $F_{rad-ocn}$ | Ocean absorbed solar radiative heat flux |
| MIZ | Marginal ice zone | | $F_{rad-owf}$ | Through-lead solar radiative heat flux |
| NSTM | Near-surface temperature maximum | | $F_{rad-underice}$ | Through-ice solar radiative heat flux |
| OML | Ocean mixed layer | | $F_S, <w'S'>$ | Kinematic salt flux |
| ONR | Office of Naval Research | | $FWC_{oml}$ | Ocean mixed layer freshwater storage |
| SAR | Synthetic Aperture Radar | | K | Extinction coefficient |
| SIZ | Seasonal ice zone | | Ri | Gradient Richardson number |
| sML | Summer mixed layer | | $Ri_{bulk}$ | Bulk Richardson number |
| wML | Winter mixed layer | | $Q_{lh}$ | Latent heat |
| YD | Year day | | $Q_{oml}$ | Ocean mixed layer heat storage |
| | | | $Q_{rad-ocn}$ | Solar radiative heat into the ocean |
| | | | $S_{ref}$ | Reference salinity (28.7 psu) |
| | | | $u_*$ | Turbulent friction velocity |
| | | | $V_{ice}$ | Ice speed |

$$u_* = (\langle u'w' \rangle^2 + \langle v'w' \rangle^2)^{0.25}, \tag{11}$$

where $<u'w'>$ and $<v'w'>$ represent the vertical transport of horizontal momentum.

Two additional quantities near the ice-ocean interface were considered. To determine periods when sufficient conditions for shear generated instabilities existed, the gradient Richardson number (Ri = $N^2/S^2$, where S is the shear) was calculated between the AOFB and ITP-V at 5.5 m. Second, the ratio of ice speed to friction velocity ($V_{ice}/u_*$) was calculated to evaluate the momentum coupling between the ice-ocean interface and the 4.5 m layer. Calculation of the drag coefficient was considered but not included, because observations at the 4.5 m level were not always indicative of the ocean/ice-interface stresses owing to near-surface stratification.

The term "ephemeral" pycnocline will be used to denote stratification present at the base of a near-surface fresh layer. Although salinity was not observed between the sea ice and the 4.5 m sensor at this site, we attempt to demonstrate the existence of the ephemeral pycnocline from estimates of turbulent parameters and freshwater storage just below this layer, and from temperature data inside the layer. A table of acronyms and math equations are provided in Table 1 for reference.

### 3.5. Sea Ice Divergence

Open water areas can expand quickly in the SIZ during summer. To distinguish periods when this expansion was driven primarily by wind conditions and not lateral/basal ice melt, surface stresses ($\tau_{total}$) were calculated from in situ observations. These surface stresses were partitioned between air-ice and ice-water interfaces following *Yang* [2006]

$$\tau_{total} = (1 - A_{OWF})\tau_{ice-water} + A_{OWF}\tau_{air-water}, \tag{12}$$

where $A_{OWF}$ is the open water fraction at C2, and $\tau_{ice-water}$ and $\tau_{air-water}$ are the ice-water and air-water stresses. Interface stresses ($\tau$) were calculated by using the drag law relationship

$$\tau = C_d |U| U, \tag{13}$$

where $C_d$ is the drag coefficient and U is the flow speed relative to the fluid. For $\tau_{air-water}$, U was estimated from the observed 2 m winds at each MIZ cluster corrected to 10 m [*Hsu et al.*, 1994]. For $\tau_{ice-water}$, U was calculated by differencing the ice speed ($U_{ice}$) from the 6.5 m ocean velocity ($U_{6.5m}$). A constant $C_d$ of 0.00125 [*Yang*, 2006] was assumed for air-water stresses and a time-varying $C_d$ was used for the ice-water stresses calculated by
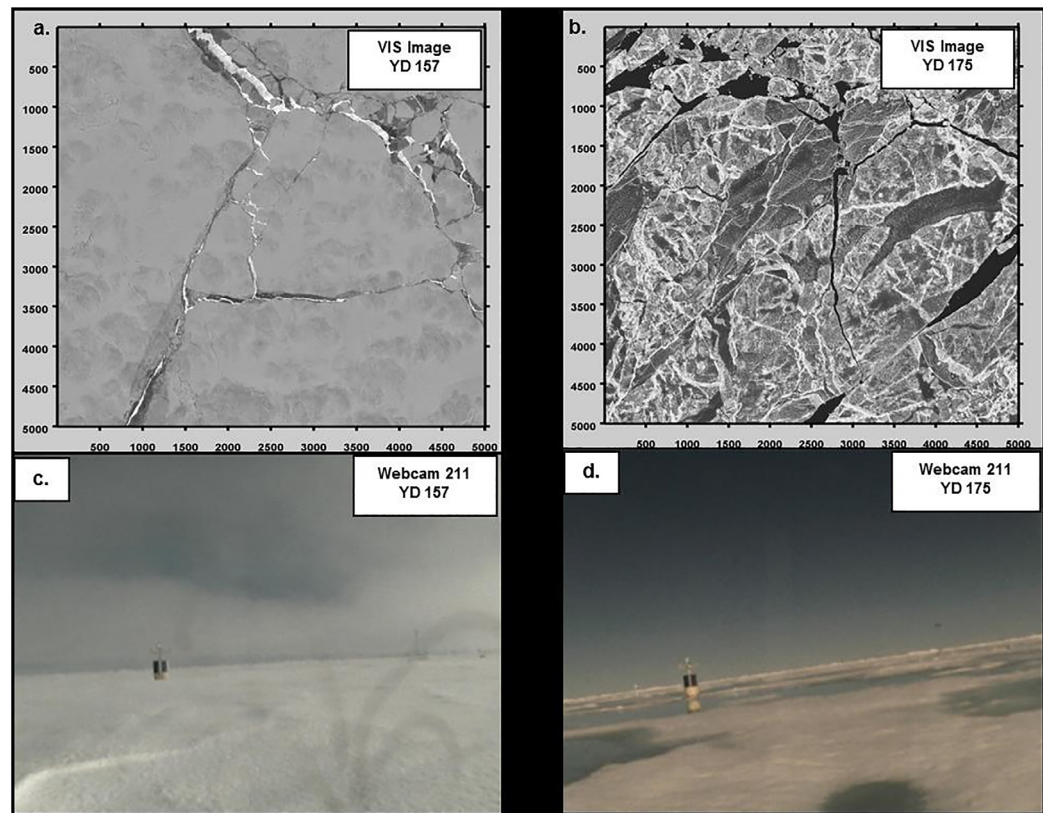
**Figure 5.** (a, b) 1 m resolution visible satellite imagery and (c, d) webcam images near C2 showing significant melt pond development during Stage I. The AOFB instrument is visible in the webcam images.

$$C_{d(6.5m)} = \frac{u_*^2}{\bar{U}^2},$$ (14)

where $u_*$ is the 6.5 m friction velocity observation from the ITP-V, and $\bar{U}$ is the 1 day mean ice-water flow speed ($U_{ice} - U_{6.5m}$). To ensure turbulence was fully developed at the 6.5 m depth, only $u_*$ values greater than 0.004 m s$^{-1}$ were used. Wind, ocean, and ice velocities were taken from the AOFBs, ITP-Vs, and AWSs deployed at clusters 2–4 and ITP-V 70. Ocean velocities were assumed zero when current data were not available. Winds were not observed at the ITP-V 70 site, thus 10 m winds from the Climate Forecast System Reanalysis were used. After surface stresses were calculated for each site, the wind stress curl was determined by

$$curl(\tau_o) = \frac{\partial}{\partial x}(\tau_{oy}) - \frac{\partial}{\partial y}(\tau_{ox}),$$ (15)

where $\tau_{ox}$ and $\tau_{oy}$ are the horizontal components of the interface stresses. We acknowledge that the orientation of MIZ instruments (Figure 1a) prevents calculation of wind stress curl directly over MIZ C2, but the calculation should provide a sufficient regional characterization of the mode (convergent ($<$0)/divergent ($>$0)) and magnitude of the wind-forced sea ice divergence.

## 4. Results

### 4.1. Stages of the Summer Evolution

The observations reported here cover a 3 month period spanning the summer evolution of the coupled ocean-ice-atmosphere system, during which the ice cover surrounding C2 changed from compact ice (winter conditions) to a fully developed MIZ (summer conditions). Although C2 drifted approximately 500 km in total across the Canadian Basin, the period from 29 June to 3 August (YDs 180–215) was dominated by largely circuitous ice motion (Figure 1a, zoomed area). During this period, the instrument array remained

within a relatively tight 100 km square region near the middle of the Canada Basin away from bathymetric boundaries. This period of the time series is important because the influence of spatial gradients were presumably limited; nevertheless, substantial changes occurred in the IOBL and OML.

We divide the summer evolution into four stages in Figures 6–10: Stage I, 30 May to 21 June (YDs 150–172), is the early summer ice-ocean boundary layer; Stage II, 22 June to 10 July (YDs 173–191), is mixed layer freshening and warming; Stage III, 11–27 July (YDs 192–208), is development of the summer mixed layer and NSTM; and Stage IV, 28 July to 19 August (YDs 209–231), is the marginal ice zone ice-ocean boundary layer. These stages were established based on the following conditions/events:

1. Stage I: Ocean mixed layer initial condition representative of spring conditions;
2. Stage I to II transition: Concurrent increases in OML heat (Figure 9a) and freshwater storage (Figure 10a), and decrease in IOBL depth (Figure 7c);
3. Stage II to III transition: Formation of the sML and NSTM (Figure 8c); and
4. Stage III to IV transition: C2 entering the MIZ defined as the buffer zone between compact ice (ice concentration > 70%) and open water ($A_{OWF} > 0.3$, Figure 6b).

In the following subsections, an overview of: sea ice conditions and radiative forcing (Figure 6), IOBL processes (Figure 7) and ice-ocean properties (Figure 8), local heat balances (Figure 9), and local freshwater balances (Figure 10) will be provided in succession for each stage.

### 4.1.1. Stage I: The Early Summer Ice-Ocean Boundary Layer

Throughout Stage I, there was very little open water, but the surface condition of the sea ice evolved substantially. Visible satellite imagery and buoy webcam images from YD 157 (Figures 5a and 5c) observed snow/ice cover with no visible surface melt water. By the end of this stage, Figures 5b and 5d confirm the development of melt ponds at C2. Although incoming solar irradiance was at its maximum during Stage I (Figure 6a), radiative flux to the ocean was small (12 W m$^{-2}$) with most entering through what little open water existed.

The IOBL exhibited near-neutral conditions with deep turbulent penetration (Figure 7c), strong air-ice-ocean momentum coupling (Figure 7d), and weak wML stratification (Figure 8d). The wML was "winter-like" with temperatures close to the in situ freezing point (Figure 8b), a thickness of about 40 m, and underlain by a strong winter pycnocline (Figure 8d). The depth of the winter pycnocline suggests that heat associated with the previous summer NSTM had been completely ventilated over the winter.
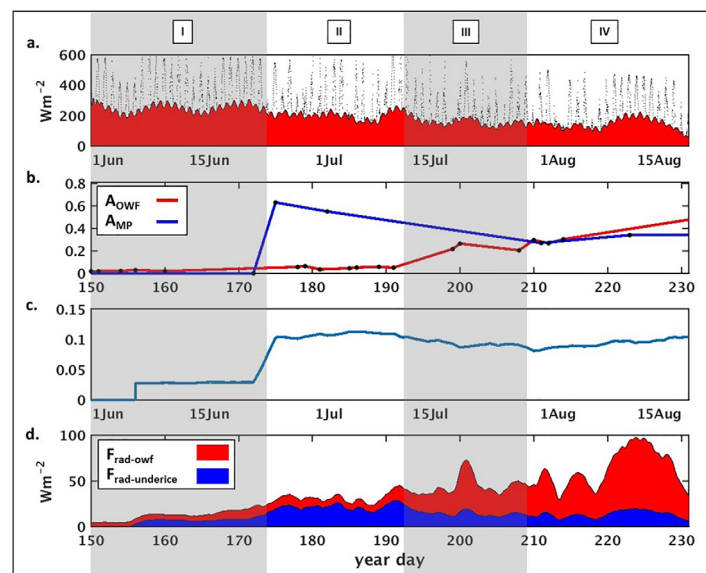
The local heat budget indicated good agreement between radiative heat input (Figure 9a, black line) and the sum of latent heat losses (blue area) and wML heat storage (gray area). Stage-averaged turbulent heat fluxes at 4.5 m were low (3 W m$^{-2}$), with only one notable event around YD 169 (45 W m$^{-2}$, Figure 9d) associated with a 10 m s$^{-1}$ wind maximum (Figure 7a). A series of deep entrainment events occurred as a result, as evidenced by the nearly 40 m maximum turbulent penetration depth (Figure 7c) and observed feathering of heat across the winter pycnocline (Figure 8b). Limited basal melt occurred (1–2 cm) demonstrating the challenge of heat exchange across a
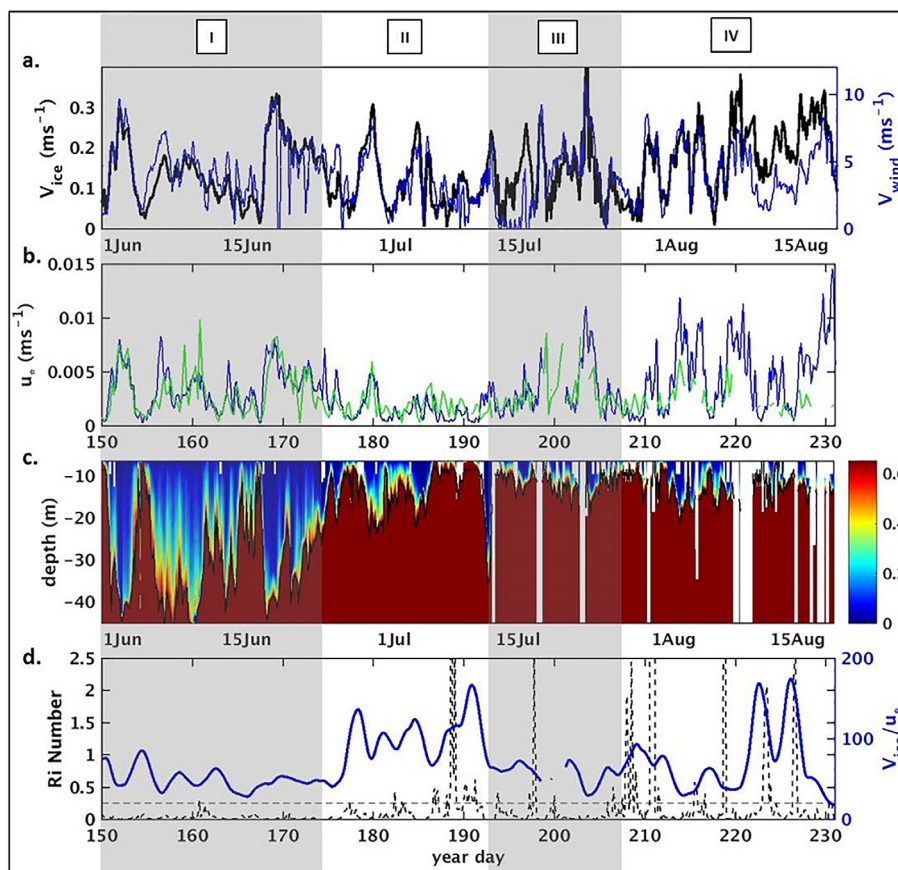


**Figure 6.** Radiative input overview at MIZ C2: (a) 3 day averaged (red area) and 15 min (black dots) incident solar irradiance observations, (b) linear interpolation of open water ($A_{OWF}$, red) and melt pond ($A_{MP}$, blue) fractions based on SAR and visible satellite imagery observations (black dots), (c) estimated sea ice transmittance ($F_{rad-underice}/F_{rad}$), and (d) 3 day averaged open-water ($F_{rad-owf}$) and under-ice ($F_{rad-underice}$) solar radiative fluxes into the ocean. Time periods of the IOBL-OML stage (I–IV) evolution are gray shaded and labeled on all overview figures.

**Figure 7.** IOBL processes overview at MIZ C2: (a) 2 m winds (blue) and ice speeds (black), (b) 4.5 m (blue) and 6.5 m (green) turbulent friction velocities, (c) bulk Richardson number ($Ri_{bulk}$) showing estimated turbulent penetration ($Ri_c = 0.65$), and (d) the ratio of ice speed to 4.5 m friction velocity ($V_{ice}/u_{*(4.5\,m)}$) (blue) and the 5.5 m Richardson number (Ri) (black).

deep winter mixed layer during the early melt season. Following the YD 169 wind event, a mesoscale front or eddy feature shoaled and weakened the winter pycnocline through the end of the stage (Figure 8d). This mesoscale activity caused a temporary imbalance in the wML freshwater budget between YDs 170 and 175 (Figure 10a). Sea ice total freshwater fluxes were low ($<1$ cm$^3$/cm$^2$ d$^{-1}$, Figure 10d); however, surface melting increased substantially toward the end of the stage (Figure 10c, light blue area), consistent with melt pond formation.

### 4.1.2. Stage II: Mixed Layer Freshening and Warming

Melt pond development continued during Stage II, leading to large increases in pond areal extent. Melt pond coverage, as determined from remote satellite imagery, exceeded 60% by YD 175 (Figure 6b). Webcam images indicate that melt pond coverage peaked on YD 178 (Figure 11a), and they subsequently confirmed melt pond drainage, with all visible surface ponds emptying by YD 187 (Figure 11b). Visible satellite imagery taken on YDs 182 and 196 further document the drainage of melt pond that occurred in the vicinity of C2 (Figures 11c and 11d). In response to expanded melt pond coverage, stage-averaged ocean radiative flux increased by 19 W m$^{-2}$ due largely to increases in the through-ice component (Figure 6d, blue area). This increase in ocean radiative flux occurred irrespective of the $\sim$50 W m$^{-2}$ decrease in stage-average solar irradiance and low $A_{OWF}$. This demonstrates how areal expansion of surface melt ponding significantly impacts solar input into the early summer OML.

The IOBL changed substantially during Stage II. The maximum depth of the IOBL, as estimated by equation (1), shoaled by almost 20 m compared to the previous stage (Figure 7c). This shoaling is probably underestimated, because changes in buoyancy above 4.5 m were not accounted for. These changes in IOBL depth occurred even though wind forcing was largely unchanged from Stage I and indicate that near-surface stratification was strongly affecting shear-related turbulent mixing. Figures 7b and 7d confirm this is the
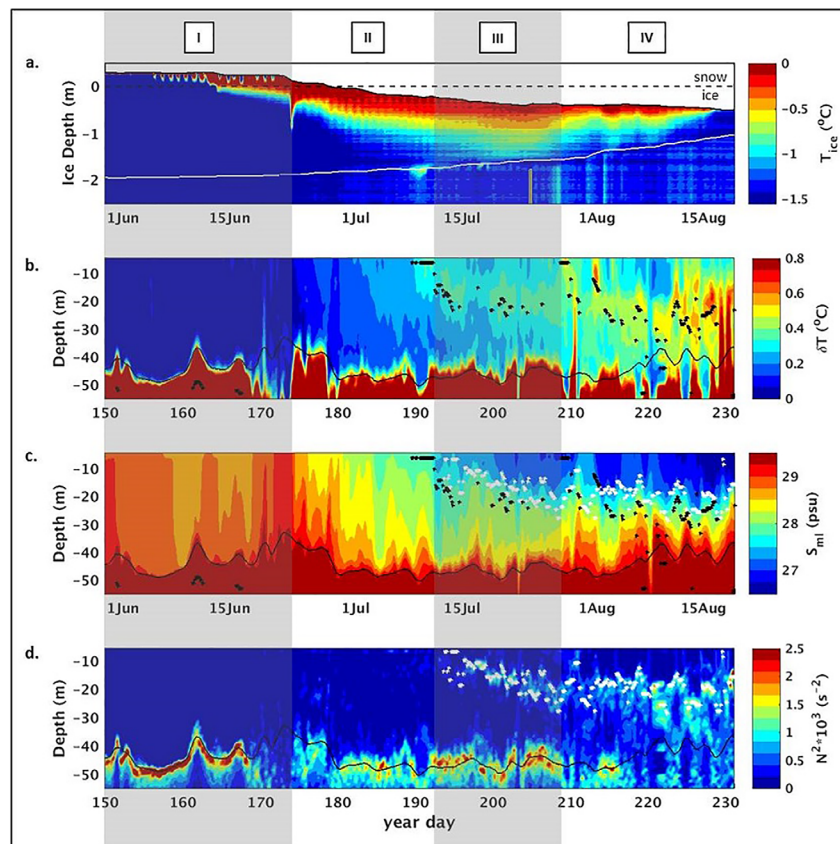
**Figure 8.** Ice-ocean properties overview at MIZ C2: (a) IMB ice temperatures with top (black) and bottom (white) interfaces, (b) upper ocean departure from freezing ($\delta$T) and depth of the NSTM (black dots), (c) upper ocean salinity, depth of summer halocline (white dots), and depth of NSTM, and (d) upper ocean $N^2$ and summer halocline (white dots). In Figures 8b, 8c, and 8d, the black line between 40 and 50 m depth represents the winter pycnocline as defined by the 1023.5 kg m$^{-3}$ isopycnal.

case with a noticeable decrease in u$_*$ and increase of V$_{ice}$/u$_*$ and Ri, particularly after YD 185. The combined surface (46 cm of snow and ice) and basal (15 cm) melt observed during the stage (Figure 8a) suggests the source of this stratification was meltwater from the sea ice. Although deepening events below the 4.5 m sensor did occur, e.g., YDs 176, 180, and 184 (Figure 7c), no significant pycnocline developed indicating that shallow stratification was periodically mixed out, but rapidly re-established after the surface stresses reduced. Few observations were available above 4.5 m to verify the increase in stratification near the surface; however, warm water ($-0.6°$C) was observed just beneath the sea ice in the IMB beginning on YD 189 (Figure 8a). Coincident with this observation was an increase in 5.5 m Ri values (Figure 7d) indicating stronger stratification near the surface. The timing of this event follows significant melt pond drainage on the sea ice surface and suggests this warm water signal was likely a melt pond drainage event to the OML via a nearby crack or flaw in the sea ice [*Polashenski et al.*, 2012]. The NSTM formed near the same date and further suggests the presence of a near-surface (ephemeral) pycnocline.

Heat budget comparisons in Figure 9a show well matched increases in both the source and sink terms during Stage II. Heat storage and latent heat fluxes were nearly equal during the stage (Figure 9c), resulting in heat equivalent increases of 39 and 41 MJ m$^{-2}$, respectively. A rough estimate of the heat content contributed by drained melt pond water shows that this was not a significant source of heat (0.3 m $\times$ 1000 kg m$^{-3}$ $\times$ 4000 J kg$^{-1}°$C$^{-1}$ $\times$ 1°C = $\sim$1 MJ m$^{-2}$) to these sink terms, implying the absorption of through-ice solar radiation was the primary heat source. Interestingly, turbulent heat flux measurements at 4.5 and 6.5 m (Figure 9d) were well below the latent heat losses observed. This suggests that most of the heat responsible for the observed basal ice melt came from solar radiation absorbed above 4.5 m depth and that mixing within this thin surface layer was frequently active. Overall, sinks exceeded source by 18% through the first two stages. Comparison of the combined sink terms in Figure 9d (gray line) shows this imbalance
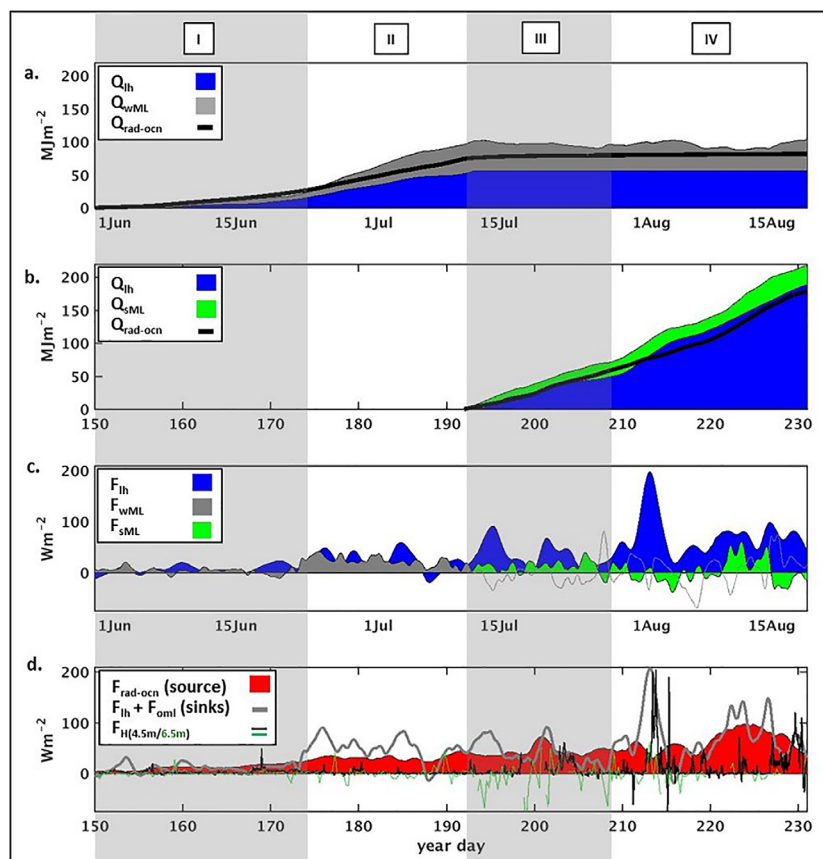
**Figure 9.** 1-D heat budget overview at MIZ C2 to estimate the magnitude of ocean absorbed solar radiation (source) and how it is redistributed between latent heat losses (sink #1) and heat storage (sink #2). (a) Winter mixed layer heat budget: 3 day averaged time series of shortwave source term $Q_{rad-ocn}$ (black line), wML heat storage sink term $Q_{wML}$ (gray), and latent heat sink term $Q_{lh}$ (blue). (b) Summer mixed layer heat budget: 3 day averaged time series of shortwave source term $Q_{rad-ocn}$ (black line), sML heat storage sink term $Q_{sML}$ (green), and latent heat sink term $Q_{lh}$ (blue). (c) The 3 day averaged latent heat flux term $F_{lh}$ (blue) and OML heat storage flux terms $F_{wML}$ (gray) and $F_{sML}$ (green), and (d) the 3 day averaged ocean radiative flux term $F_{rad-ocn}$ (red), sum of latent heat and OML heat storage flux terms $F_{lh} + F_{oml}$ (gray line), and turbulent heat fluxes at 4.5 and 6.5 m ($F_{H(4.5m/6.5m)}$, black and green lines, respectively).

occurred while melt ponds were present around the C2 sensors (YDs 175–187) indicating through-ice radiative flux (equation (4)) was likely underestimated during this period. This may have been the consequence of IMB sensors being deployed preferentially in thick ice (for survivability) resulting in $z_{ice}$ in equation (4) being greater than the larger area mean ice thickness.

Consistent with the melt pond drainage observed, freshwater flux from the sea ice surface was the highest of any stage (Figure 10c). Turbulent freshwater fluxes at 4.5 m show that these increases to wML freshwater storage were well correlated with the mixing events on YDs 176, 180, and 184 (Figure 10d). In general, increases to OML freshwater storage exceeded the total freshwater inputs from the sea ice (Figure 10d, gray line). This resulted in a 0.36 m imbalance in the freshwater budget at the end of Stage II (Figure 10a). Figure 8c suggests that this imbalance at the end of the stage was enhanced by the brief passage of a fresh mixed layer front around YD 191. The imbalances observed earlier in the stage were likely the result of a combination of lateral advections and the challenge of single point IMB observations in capturing the areal mean meltwater flux from a heterogeneous ponded sea ice surface.

### 4.1.3. Stage III: Development of the Summer Mixed Layer and NSTM

During Stage III, melt pond coverage decreased to less than 40% and $A_{OWF}$ increased from 5% to 26% (Figure 6b). The 21% increase in $A_{OWF}$ occurred in just 9 days (YDs 191–200) and was coincident with a significant increase in positive wind stress curl around YD 193 (Figure 12a). Divergence of the sea ice resulted in a stage-to-stage average increase of 14 W m$^{-2}$ in ocean absorbed solar radiation (Figure 6d) and highlights the importance of winds to the heat balance in late summer.
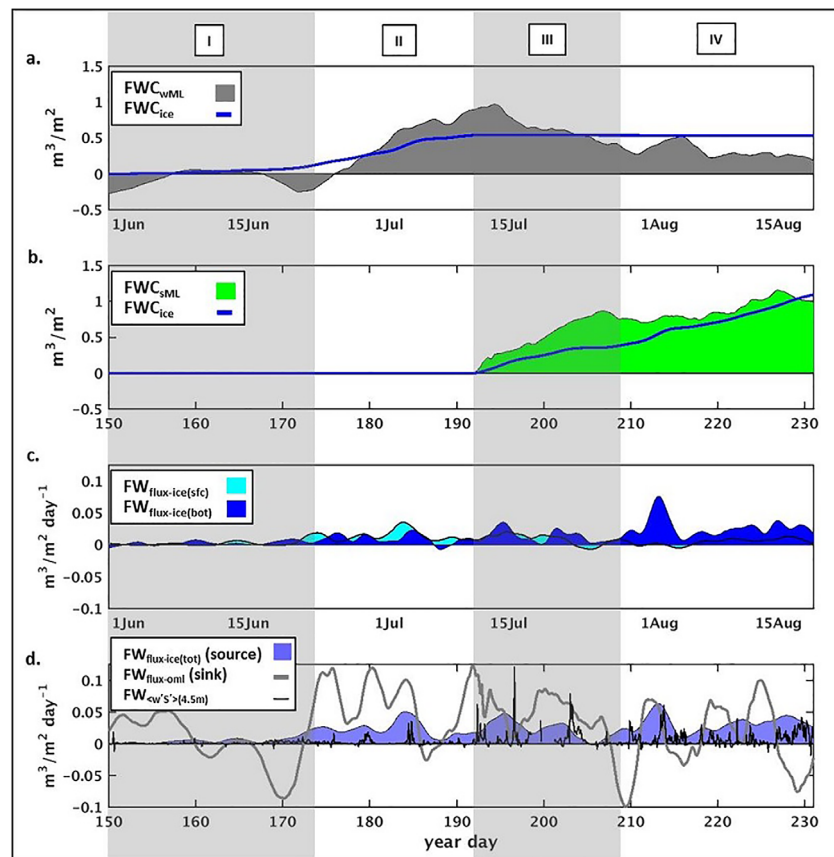
**Figure 10.** 1-D freshwater budget overview at MIZ C2 to compare freshwater input from the sea ice to freshwater storage in the upper ocean. (a) Winter mixed layer freshwater budget: 3 day averaged integrated freshwater flux from top and bottom ice melting term $FWC_{ice}$ (source term, blue line) and wML freshwater storage sink term $FWC_{wML}$ (gray). (b) Summer mixed layer freshwater budget: 3 day averaged integrated freshwater flux from top and bottom ice melting term $FWC_{ice}$ (source term, blue line) and sML freshwater storage sink term $FWC_{sML}$ (green). (c) 3 day averaged freshwater flux from melting of the sea ice surface ($FW_{flux\text{-}ice(sfc)}$, light blue) and the sea ice bottom ($FW_{flux\text{-}ice(bot)}$, dark blue). (d) 3 day averaged total freshwater flux from the sea ice ($FW_{flux\text{-}ice(tot)}$, purple area), OML freshwater storage fluxes ($FW_{flux\text{-}oml}$, gray line), and freshwater fluxes inferred from turbulent salt fluxes at 4.5 m ($F_{<w's'>(4.5m)}$, black line).

The IOBL and OML transitioned to summer conditions with the formation of the sML. In the IOBL, moderate wind forcing deepened the turbulent mixing layer just after the start of Stage III (Figure 7c). Overall during this stage, momentum fluxes increased (Figure 7b) and the ratio of $V_{ice}/u_*$ decreased (Figure 7d) to Stage I values showing well mixed conditions down past the 4.5 m sensor depth. In the OML, a secondary $N^2_{max}$ appeared in the upper 15 m around YD 192 (Figure 8d), consistent with freshwater from the surface mixing down, and marked the development of the sML and associated summer halocline. Initially, the summer halocline was weak and its depth was variable, alternating between 4.5 and 15 m. By YD 196, it became more defined and steadied at a depth of about 10 m. The sML deepened by $\sim$1 m d$^{-1}$, to 20 m by the end of Stage III, which was reasonably consistent with the maximum turbulent penetration estimates (Figure 7c). As expected, the NSTM, which was present just prior to sML development, remained just below the new sML in the summer halocline (Figure 8c).

Latent heat losses dominated the local heat budget following the onset of summer conditions. As expected, the increase in turbulent mixing and open water areas during this period resulted in larger stage-averaged basal melt rates (1.1 cm d$^{-1}$). Not expected, however, was the decrease in wML heat storage. The NSTM layer, located in the summer halocline stratification at the top of the wML, was assumed to be dynamically isolated from the ice. NSTM heat storage was expected to be retained and slowly increase as small amounts of penetrating solar radiation warm the layer, yet wML observations showed heat storage losses. These heat storage losses were small ($\sim$8 MJ m$^{-2}$, Figure 9a) and may have been the result of weak lateral advections; however, Figure 9c shows modest heat losses (gray line) associated with the YD 196 and 203 mixing events. This suggests a portion of the wML heat loss may have been due to a deepening sML. Negative turbulent heat fluxes were observed at
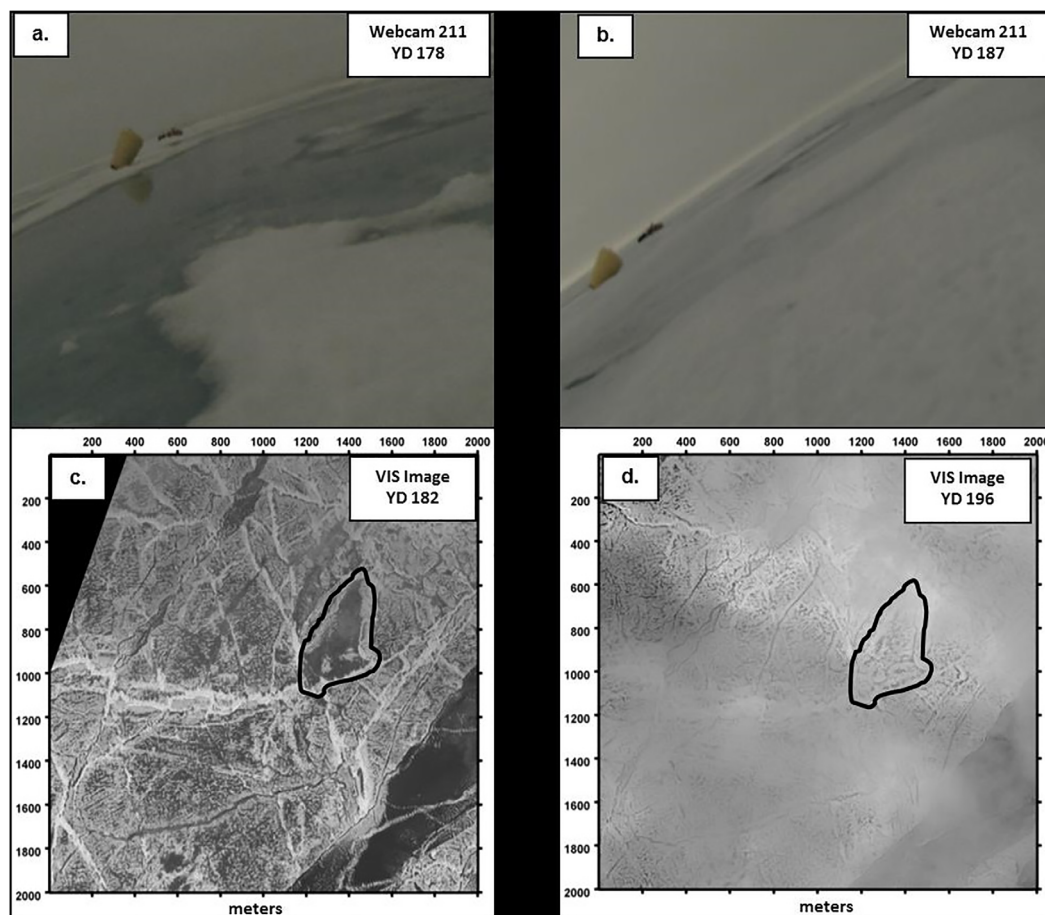
**Figure 11.** Webcam images from C2 showing (a) peak melt pond coverage on YD 178, and (b) full melt pond drainage by YD 187. Visible satellite imagery taken on YD 182 (c) and YD 196 (d) also show extensive melt pond drainage in the areas surrounding C2. The area outlined in black in Figures 11c and 11d highlights a large melt pond that drained by YD 196.

the 6.5 m sensor (Figure 9d, green line) during weak winds and negative dT/dz. The cause of these negative heat fluxes are not explicitly known, but were likely the result of small scale reversals in the local temperature gradient as the sensor passed through the developing summer halocline. Overall, the 1-D heat budget essentially balanced during Stage III with radiative input exceeding the combined sink terms by only 4%.

Immediately after the summer halocline developed, between YDs 192 and 194, freshwater storage in both the wML and sML increased, 6 and 20 cm, respectively (Figures 10a and 10b). This suggests that roughly $\sim$0.25 m of melt water was mixed down from the near-surface layer above 4.5 m to facilitate summer halocline formation. This is further evident by the high turbulent freshwater fluxes observed when wind-driven forcing generated sufficiently strong turbulence (Figure 10d) to mix the near-surface fresh layer down past the AOFB sensor. In fact, the highest kinematic salt flux of the time series occurred around YD 196 of $\sim$4 $\times$ $10^{-5}$ psu m s$^{-1}$, the equivalent of 0.12 m$^3$/m$^2$ d$^{-1}$, and was coincident with the observed strengthening of the summer halocline on that same date.

### 4.1.4. Stage IV: Marginal Ice Zone Ice-Ocean Boundary Layer

By the start of Stage IV, $A_{OWF}$ had increased to 0.3 and rapidly expanded to almost 0.5 by the end of time series (Figure 6b) when the instruments were essentially in open water. Stage-averaged incoming solar irradiance was $\sim$100 W m$^{-2}$ less than that of the summer solstice maximum (Figure 6a), but stage-averaged radiative heat fluxes into the ocean increased fivefold to 63 W m$^{-2}$ as a direct result of larger open water areas. A little less than 50% (121 MJ m$^{-2}$) of the total ocean radiative input for the melt season occurred during Stage IV. Basal melt rates were irregular with a single 4 day event (YDs 211–215) responsible for 32% (17 cm) of the stage melt (Figure 8a). Outside of this event, melt rates were steady averaging 1.9 cm d$^{-1}$ and resulted in 52 cm of total melt during the final stage.
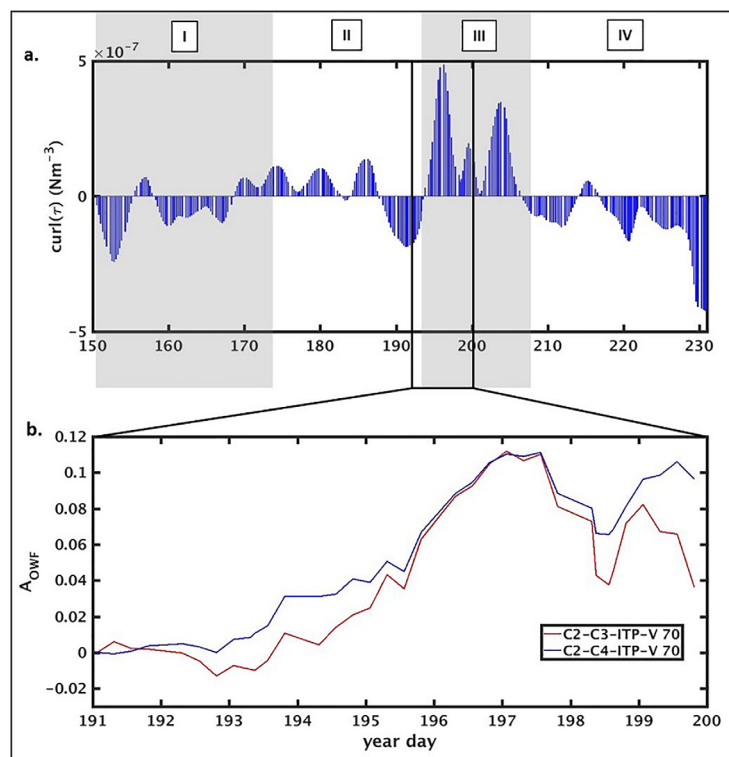
**Figure 12.** (a) 2 day averaged wind stress curl (curl($\tau$)) estimated from MIZ C2-C4 and ITP-V 70 observations in the Canada Basin. (b) Estimation of open water fraction ($A_{OWF}$) from divergence between the MIZ sensors using the triangle area differencing method [*Stanton et al.*, 2012]. Triangle area differencing was calculated on C2, C3, and ITP-V 70 (red) and C2, C4, and ITP-V 70 (blue).

Several warm pulses were observed in the sML during the first 7 days of the stage (Figure 8b). Wind forcing was sporadic (Figure 7a), with predominately weak winds interrupted by moderate events. As expected, large heat fluxes resulted from these conditions, often exceeding 100 W m$^{-2}$ (Figure 9d). After YD 215, u$_*$ observations (Figure 7b) indicate the sML was strongly mixed; however, the strength of the summer halocline stratification constrained the sML to a relatively thin layer (15–20 m). During weak winds, however, 5.5 m Ri values (Figure 7d) exceeded the critical value (0.25) on several occasions during the stage. This suggests that strong basal melt during Stage IV facilitated the development of near surface fresh layers and ephemeral pycnoclines, but these were 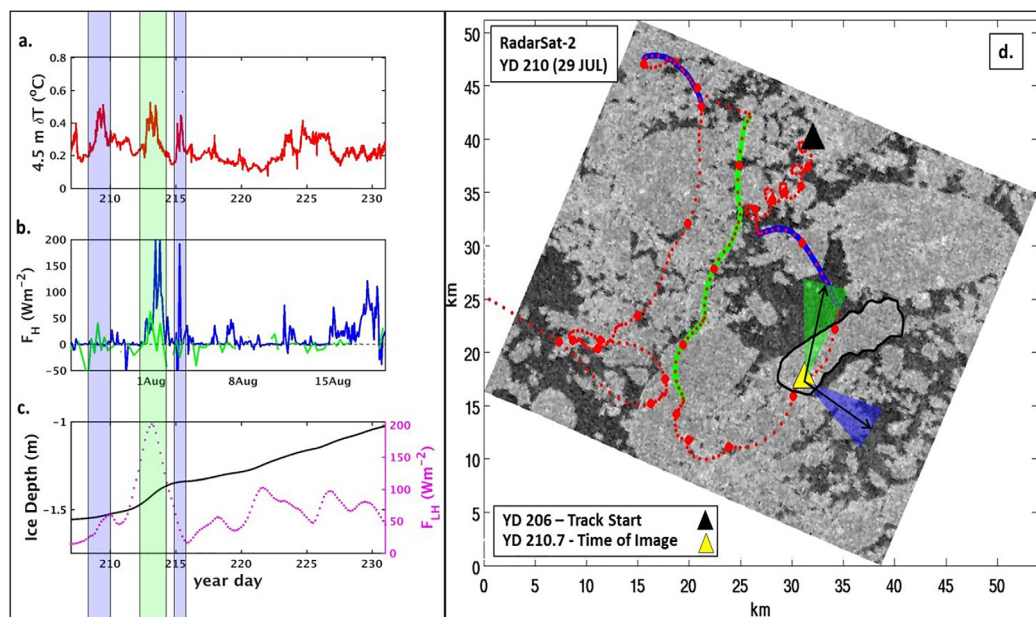quickly mixed out when interface stresses increased. After YD 220, these near-surface fresh layers seemed to prevail and supported "slippery layers" as seen in the large increase in ice speed relative to wind speed (Figure 7a) and increase to V$_{ice}$/u$_*$ ratios (Figure 7d). This is further validated by the near-surface warming (Figure 8b) and 14 MJ m$^{-2}$ increase in sML heat storage observed between YDs 221 and 227 (Figure 9b). These near-surface fresh layers are less evident in the IMB temperature data (Figure 8a) due to the higher ice speeds (Figure 7a) which mix the limited basal melt water through the 1–4.5 m volume. In general, turbulent fluxes were highly variable in this strongly stratified MIZ environment with large friction velocity variations ($\sigma^2_{IV} = 2.5\sigma^2_{I-III}$) and occasional large turbulent heat fluxes (maximum F$_H$ = ~200 W m$^{-2}$).

The 1-D heat budget remained reasonably balanced throughout most of the final stage, with the exception of the large melting event between YDs 211–215. Figure 9d highlights this imbalance in the local heat budget, during which observed sink fluxes (gray line) exceeded radiative source fluxes by nearly 70 W m$^{-2}$ on average over the 4 days (peak imbalance = 148 W m$^{-2}$). This imbalance integrated to 24 MJ m$^{-2}$ over the period and was accompanied by large turbulent heat fluxes. Moderate turbulent heat fluxes (50–100 W m$^{-2}$) were observed at the end of the stage as well, but appeared to be due to higher u$_*$ and OML heat storage values.

Overall, freshwater storage decreased during the final stage (Figure 10a) as a result of increased wML salinity and wML thinning. Investigation of Figures 8b–8d indicates that these changes were likely the result of winter pycnocline weakening allowing salt and heat to diffuse into the wML above. Unlike previous stages, turbulent freshwater fluxes were less intermittent as result of the increased mixing in Stage IV and compared reasonably well to total freshwater fluxes from the sea ice (Figure 10d).

## 4.2. Enhanced Basal Ice Melt Event

A significant basal ice melt event occurred between YDs 211–215 associated with large turbulent heat fluxes (Figure 9d). This suggests that two different IOBL-OML regimes existed during the MIZ Stage, one supporting

**Figure 13.** MIZ upstream conditions (CASE I): (a) 4.5 m $\delta$T, (b) 4.5 m (blue) and 6.5 m (green) turbulent heat fluxes, (c) 3 day averaged sea ice bottom interface depth (black) and latent heat fluxes (magenta dots), and (d) RadarSat-2 image (YD 210.7) overlaid with MIZ C2 GPS track (red dots) between YD 206 (black triangle, start time of time series plots in Figures 13a, 13b, 13c) and YD 216. The time periods of interest are color coded in blue and green along the GPS track and on the corresponding supporting plots (a, b, c). To determine the direction of ice motion during the different time periods, color coded vector triangles with direction arrows are plotted over the location of C2 at the time the image was acquired (yellow triangle).

the predominate mean melt rate ($\sim$1.9 cm d$^{-1}$) and another supporting the enhanced melt rate ($\sim$4.3 cm d$^{-1}$). To investigate, we considered two case studies within Stage IV under different conditions. The goal was to characterize conditions upstream of MIZ C2 to determine factors that led to the short-term imbalances in the local heat budget. This was done by overlaying GPS tracks of C2 over Radarsat-2 imagery (Figures 13d and 14d). Since Radarsat-2 imagery was only available every 5 days or so, several days of track information were plotted on a single image (red track). This limitation required that we assumed the ice field around C2 is "frozen," i.e., the general fraction and direction of open water around the C2 ice floe did not change during the case study. Additionally, we ignored upper ocean currents since the distances between C2 and the adjacent leads were small (<5 km) and ice speeds were large compared to ocean currents. To orient the reader on the direction of C2 ice floe motion, vector triangles with direction arrows are placed over the C2 position when the image was acquired and are color coded to the appropriate GPS track sections. These same color codes were overlaid on adjacent supporting plots to associate in situ observations to the specific track periods.

CASE I examines the period between YDs 206 and 216 to study the temporary condition that supported high basal melt rates (Figure 13). Beginning on YD 206 (Figure 13d, black triangle marker), C2 moves southwestward along a classic inertially oscillating track leading up to the YD 211–215 event. Substantial peaks in the 4.5 m $\delta$T were observed on YDs 209, 213, and 215 (Figure 13a). These peaks correlate well to periods when C2 was moving in the direction of large open water areas around the C2 ice floe (Figure 13d). These observations suggest that during periods of slow ice motion, differential heating of the ice-covered and open-water upper ocean generated small horizontal scale temperature gradients in the sML budget control volume. Large turbulent heat fluxes (>150 W m$^{-2}$, Figure 13b) occurred when the sea ice moved over these warm open water areas resulting in significant latent heat fluxes (Figure 13c). This suggests that basal melt was spatially variable during these thermally heterogeneous conditions, and was strongly dependent on the time history of ice floe displacements relative to open water areas directly around the ice floe. The substantial heat imbalance observed between YDs 211 and 215 (Figure 9d, gray line) indicates that the areal scale (45 km square) of the satellite products used to estimate $F_{rad-ocn}$ were too large during these condition. For example, to estimate the appropriate incoming ocean radiative flux for the YD 211–215 event, the $A_{OWF}$ would have to be almost tripled from 30% to 80% in equation (3). This is the approximate $A_{OWF}$ of the 10 km square area just north of the ice floe seen in Figure 13d.
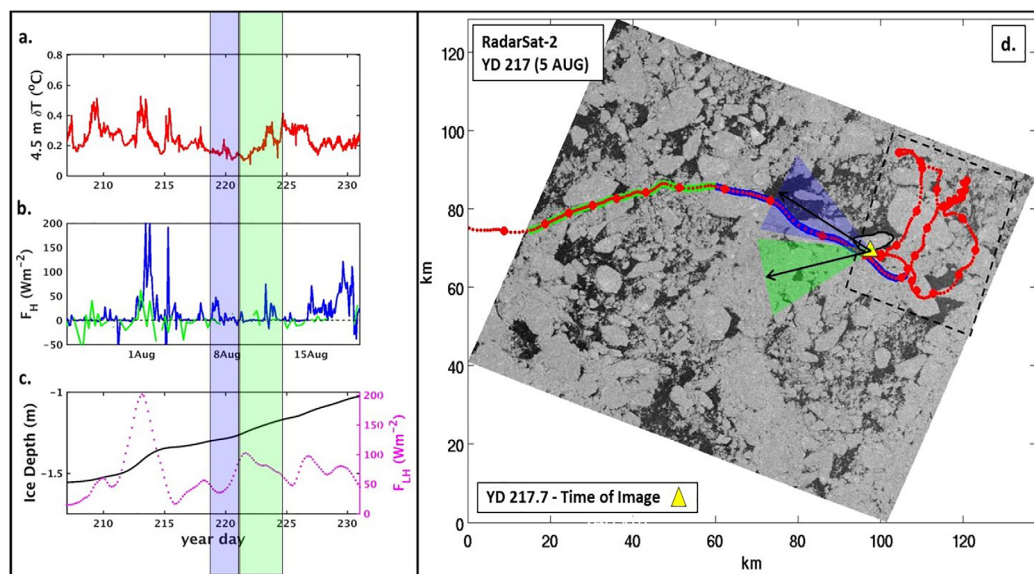
**Figure 14.** MIZ upstream conditions (CASE II): same format as Figure 13 for a RadarSat-2 image taken on YD 217.

CASE II (Figure 14) investigates the period between YDs 218 and 225 to study the predominate condition that supported the mean melt rate. Observations indicate that changes occurred in both the wind forcing and ice-ocean system over this period. Ice speeds increased around YD 218 ($\sim$20 cm s$^{-1}$), and ice direction became persistently westward. A black box is drawn around the 10 day track of the previous case (Figure 14d, upper right) to highlight the large change in ice motion character and spatial scale between the two events. Although C2 moved toward a large area of open water between YDs 219 and 221 (Figure 14d, blue cone), 4.5 m $\delta$T observations were virtually unchanged (Figure 14a) indicating upstream conditions were homogeneous. Momentum fluxes were large during this period, yet basal melt rates and turbulent heat fluxes (Figures 14b and 14c) remained low compared to the previous heterogeneous case study, and had little dependence on upstream surface conditions. These findings suggest that during persistent, moderately strong ice motions, the sML thermal structure is horizontally homogeneous to the first order due to the redistribution of lateral temperature gradients in response to increased mixing and stirring.

### 4.3. Summer Season Overview

In the previous section, we estimated local budgets during each stage of the summer evolution; however, it is important to integrate these budget terms over the entire summer to determine the influence each had on the overall IOBL-OML system. At MIZ C2, a total of 261 MJ m$^{-2}$ of heat was estimated to have entered the ocean, with 64% entering through leads ($F_{rad-owf}$) and 36% penetrating through the ice ($F_{rad-underice}$). About 65% of the through-ice component was estimated to have come through surface melt ponds, primarily during Stage II. The local heat budget (Figure 9) shows that heat input was partitioned unevenly in the IOBL-OML system, with 77% distributed to latent heat losses (247 $\pm$ 6 MJ m$^{-2}$) and 23% toward OML heat storage gains (75 MJ m$^{-2}$), similar to the findings of *Toole et al.* [2010]. Sea ice top and bottom interface losses were roughly equal, with 80 $\pm$ 2 cm (30 cm (snow)/50 cm (ice)) of surface ablation and 91 $\pm$ 2 cm of basal ice melt.

Given the long duration (81 days) and large spatial distances covered ($\sim$500 km), the heat balance closed relatively well, with sink terms exceeding the estimated radiative source term by 19%. Almost half of this imbalance (24 MJ m$^{-2}$) came from the YD 211–215 melting event. This suggests that at least 89% of the total OML heating came from local radiative fluxes. The remaining 11% was likely a combination of through-ice radiative parameterization errors and advection of heat from outside the OML control volume. These results are slightly higher than the 0.8/0.2 partitioning found by *Steele et al.* [2010] in the Pacific Sector of the Western Arctic. These differences are likely due to the geographic location of the current study away from the strong ocean currents near the Bering Strait and north coast of Alaska that influence the
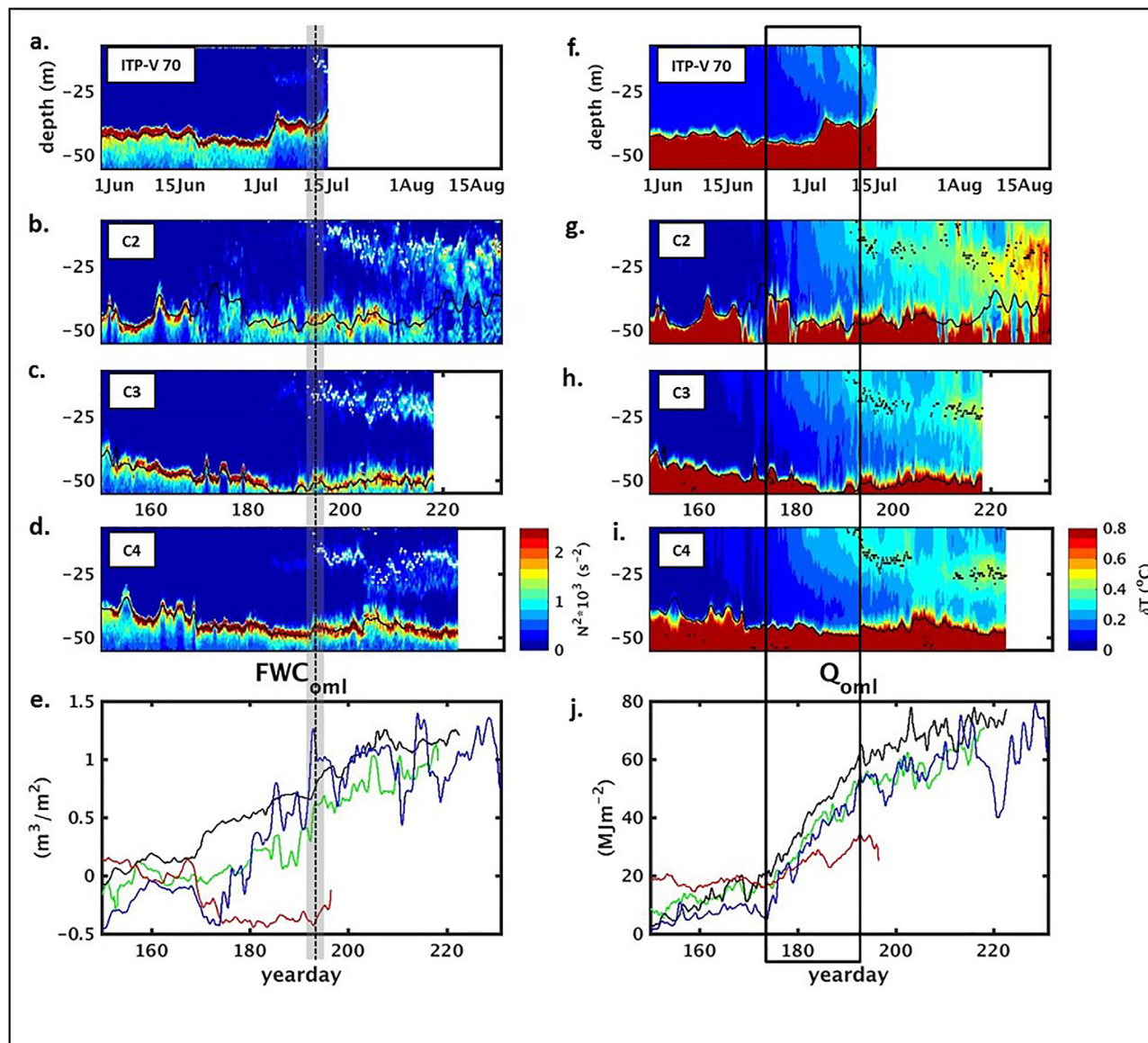
**Figure 15.** Regional comparisons of (a) ITP-V 70, (b) C2, (c) C3, and (d) C4 of upper ocean $N^2$ and summer halocline depth (white dots), and (e) OML freshwater storage for ITP-V 70 (red), C2 (blue), C3 (green), and C4 (black). Vertical dashed line indicates date of summer halocline development (~YD192). On the right hand side (f, g, h, i), corresponding upper ocean $\delta T$ and NSTM (black dots), and (j) OML heat storage are presented. Black box highlights the Stage II period of the summer evolution (YDs 173–192).

Pacific Sector. In summary, these results indicate the changes observed in the late summer Canada Basin SIZ are primarily driven by local thermodynamic process.

### 4.4. Regional Variability of the Summer Evolution

To determine the regional variability of the summer evolution across the Canada Basin, the findings from C2 are compared to the ITP-V 70, C3, and C4 locations (see Figure 1a). Upper ocean $N^2$, freshwater storage, and heat storage were evaluated for each site and are presented on Figure 15. These results were analyzed using methods defined in section 3 with the exception of the upper limit of integration for the budget control volume was adjusted to the shallowest ITP-V observation (6 m).

The date of sML development showed remarkable consistency across the Canada Basin. The vertical dashed line in Figures 15a–15d shows that the summer halocline appeared at all sites around YD 192 (±1 day) and with roughly the same pace of initial deepening. The average depth of the summer halocline, evaluated for each station between YDs 192 and 218, showed increasing depths toward the east (C2 = 17.6 m,
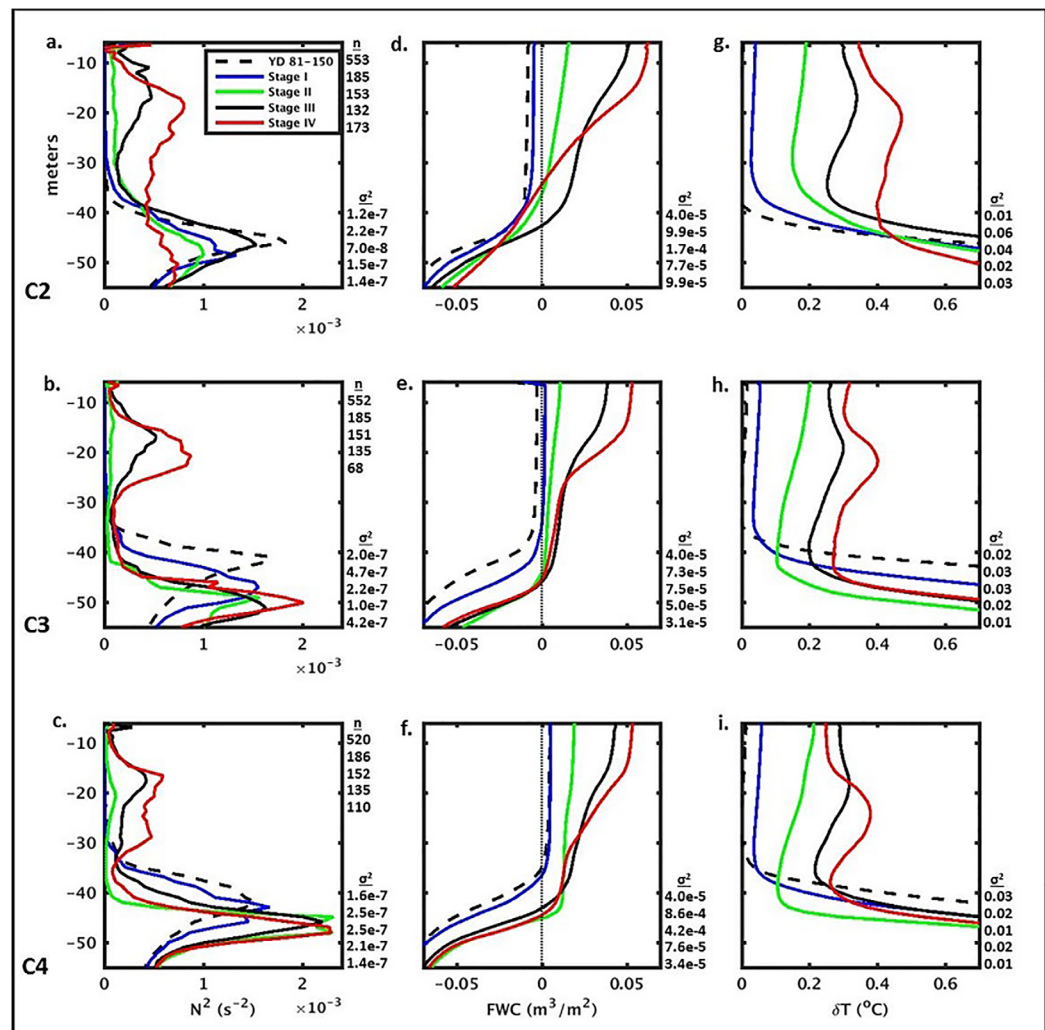
**Figure 16.** Upper ocean profiles of stage-averaged (a, b, c) $N^2$, (d, e, f) freshwater storage (FWC), and (g, h, i) $\delta T$ for clusters 2–4 (see legend). Rows correspond to observations from C2, C3, and C4, respectively. Number of profiles (n) and the mean variance statistics ($\sigma^2$) across all depths for each stage are provided on the right side of the plot.

C3 = 19.3 m, and C4 = 19.9 m). These differences in sML depth appear to be the result of stronger mixing and weaker stratification at C3 and C4. Estimates of ice-water drag, using equation (14) during near-neutral conditions (March to May), indicate that $C_{d(6.5m)}$ at C3 and C4 (4.6 and $5.9 \times 10^{-3}$) were significantly larger than $C_{d(6.5m)}$ values at C2 ($3.0 \times 10^{-3}$). Additionally, mean OML $N^2$ after YD 192 was lower at C3 and C4 (1.8 and $2.4 \times 10^{-4}$ s$^{-2}$) as compared to C2 ($3.2 \times 10^{-4}$ s$^{-2}$). This is consistent with the longitudinal orientation of the clusters in early season, with C4 furthest north ($\sim$75°N) and C2 furthest south ($\sim$73°N). This likely placed C4 in a region of more deformed multiyear ice and C2 in a younger thinner mixture of multiyear ice and first-year ice. This hypothesis is further supported by the temporary disappearance of the NSTM at C3 and C4 (Figures 15h and 15i) during the YD 203 mixing event.

Figure 15e shows similar increases in OML freshwater storage at C2–C4 during the Stage II period of the IOBL-OML evolution. However, the rate of freshwater storage increase at C3 and C4 was slower and may have been the result of the variability in sea ice type/condition mentioned previously. Differences in sea ice age can effect melt pond coverage [*Perovich et al.*, 2002; *Perovich and Polashenski*, 2012] and possibly affect the rate at which drainage occurred locally [*Polashenski et al.*, 2012]. ITP-V 70 showed very little correlation to the other sites. The large salinity increases observed at this site around YD 166 (not shown) suggests these differences were possibly due to a lateral front as this site approached the Northwind Ridge. These results suggest that melt ponds drained to the upper ocean on comparable time scales across the Canada Basin SIZ.

OML heat storage comparisons showed even stronger similarities. Figure 15j shows that the large heat storage gains observed at C2 during Stage II of the summer evolution (black box) were also observed at C3 and C4 with nearly identical timing and magnitude. These increases of heat storage were even observed at ITP-V 70, some 250–500 km (depending on YD) northwest of C2. As was the case for C2, heat storage increases at C3 and C4 during Stage II accounted for ∼50% of the total time series heat storage gain. Likewise, the NSTM developed at C2, C3, and C4 around YD 190 and immediately prior to sML development. Flattening of the OML heat storage curve after YD 192 at C2-C4 indicates that the shift in heat partitioning away from heat storage and toward latent heat losses was part of a regional, not local, IOBL-OML system change. Heat storage gains between YDs 192 and 218 at C3 and C4 were comparable to C2 and consistent with the estimated radiative input expected below the summer halocline depth ($<1$ MJ d$^{-1}$, following *Frey et al.* [2011]). These results show that redistribution of radiative input within the IOBL-OML system evolved in similar ways across the Canada Basin SIZ throughout the 2014 summer season.

Stage-averaged profiles of N$^2$, freshwater storage, and $\delta$T for C2, C3, and C4 are presented in Figure 16 for a more comprehensive look at the temporal changes in stratification and OML heat content. These results show that changes in the upper ocean profiles are essentially equal through the first three stages of the evolution at each site. This demonstrates that each of the first three stages were distinctive and occur on similar time scales and magnitudes, regardless of their geographic location in the Canada Basin SIZ.

Stage IV also showed unique profiles at all sites with a prominent summer halocline and NSTM; however, some differences do exist. For instance at C2, the NSTM is slightly warmer and the sML is fresher than at the other two sites. Additionally, C2 was saltier and warmer in the layer beneath the sML and above the winter pycnocline. This was likely due to weakening of the winter pycnocline stratification (Figure 16a), permitting salt (Figure 16d), and heat (Figure 16g) to diffuse upward. During strong mixing between YDs 229 and 231, the sML deepened into this warm layer (Figure 15g) resulting in 4.5 m turbulent heat fluxes of ∼100 W m$^{-2}$ (Figure 9d). These results suggest that upper ocean properties during late summer have some dependency upon their location in the SIZ. This dependency is likely a result of the large variability in open water fraction across the MIZ, which in turn drives changes in basal melt rates and the degree of air-ocean interaction.

## 5. Discussion

### 5.1. Causes and Consequences of the IOBL-OML Evolution

The IOBL and OML evolved through four distinct regimes during the summer melt season. In this section, we explore the geophysical forcing responsible for stage development and the influences these forcings have on the larger coupled ice-ocean system.

### 5.1.1. Early Season Influences: Melt Ponds

Melt ponds strongly affected the underlying ocean during early summer. Melt pond development at the beginning of Stage II increased through-ice radiative fluxes, allowing more sunlight to penetrate through the ice cover. This increase in thermal forcing doubled basal melt rates as compared to Stage I. By itself, however, this increased solar heat input did not substantially change the character of the IOBL, because interface stresses were still able to mix the near-surface stratification generated by basal melting throughout the larger wML volume (refer to process schematic Figure 17).

As melt ponds began to drain after YD 178, freshwater storage in the ocean mixed layer exceeded the amount provided by basal melting. This enhanced freshwater input from melt pond drainage immediately affected the dynamics of the IOBL. Mixing at and below the 4.5 m observation depth was greatly reduced (Figure 7b), suggesting that the IOBL shoaled to depths above the observation level. The shoaling of the IOBL brought the residual portion of the wML closer to ice-ocean interface, which then warmed due to the stronger radiative fluxes near the surface.

The upper ocean gained a significant amount of heat in the 19 days leading up to NSTM development. In the wML, 39 MJ m$^{-2}$ of heat accumulated during this period (Stage II), accounting for 52% of the total OML heat storage observed for the summer. These results are consistent with summer observations from previous Canada Basin studies of melt pond evolutions [*Perovich et al.*, 2002, 2007b; *Perovich and Polashenski*, 2012] and upper ocean heat content [*Jackson et al.*, 2010; *Toole et al.*, 2010; *Jackson et al.*, 2012; *Timmermans*, 2015], which when compared together, shows that melt pond development and drainage are roughly coincident with the large OML heat storage gains observed in mid-to-late June. We believe that the similarities between this study
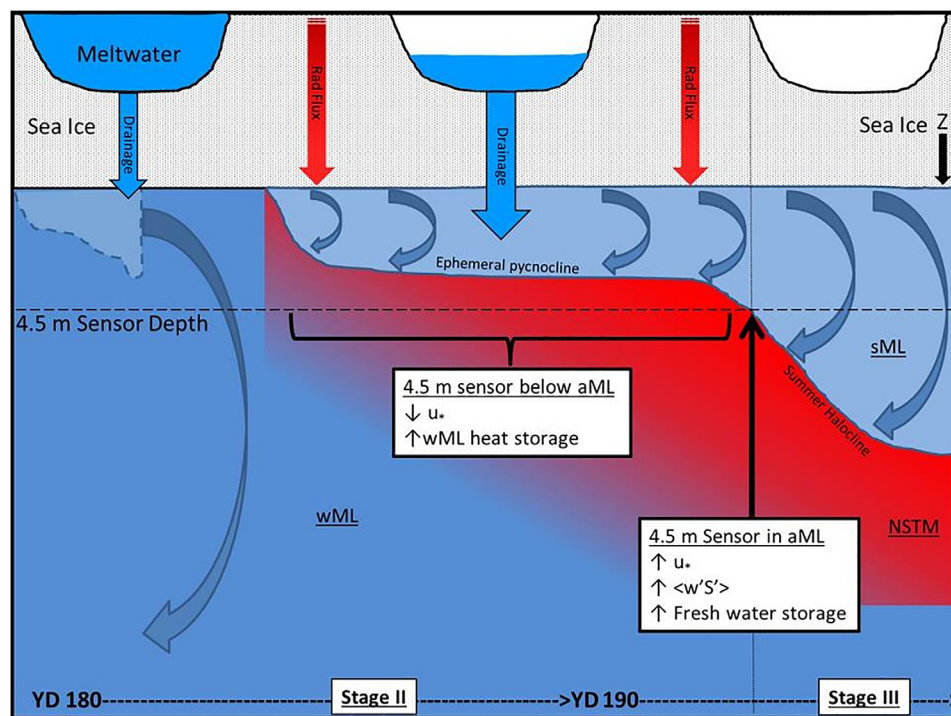
**Figure 17.** A depiction of the sea ice and the upper ocean showing the influence drained melt pond water had on the IOBL-OML system between YDs 180 and 195. Initially, small amounts of melt water are easily mixed out during wind events (between about YD 180 and 185, left side of cartoon). As melt water input to the OML increased, primarily due to melt pond drainage, the active mixing layer (aML) contracts resulting in substantial wML heat storage gain, and development of the NSTM (middle portion of cartoon). Following melt pond drainage, the sML develops during the subsequent wind event as turbulent processes deepened the fresh, near-surface mixing layer below the shallowest sensor (4.5 m), resulting in immediate increases to $u_*$, salt flux ($<w'S'>$), and sML freshwater storage (right side of cartoon).

and previous work provides strong evidence that the early summer upper ocean evolution observed in this study occurs each summer and is closely linked to the evolution of melt ponds in the Canada Basin SIZ.

Linkage of the melt pond evolution with the early summer upper ocean evolution raises interesting questions about the variability of radiative input to the ocean under different ice types. *Perovich and Polashenski* [2012] show that seasonal sea ice has substantially larger melt pond coverage areas (as high as 0.7) and much smaller albedos (as low as 0.32) as compared to multiyear ice (0.3–0.4 and 0.5, respectively). Given these large differences between multiyear and seasonal sea ice and the high solar irradiance in early summer, we speculate that early summer OML heat storage will increase as the Canada Basin SIZ sea ice becomes younger.

### 5.1.2. Summer Mixed Layer and NSTM Development

The sML developed on YD 192 during a modest wind event (7 m s$^{-1}$, Figure 7a). Interestingly, a similar wind event on YD 184 did not create a substantial near-surface N$^2$ maximum. This difference in response suggests that insufficient freshwater was available to develop the summer halocline between the YD 180 and YD 184 mixing events. Following the YD 184 mixing event, calm winds prevailed until the sML developed on YD 192. Although few observations exist above 4.5 m, several observations suggest the presence of a thin, fresh actively mixing layer above a near-surface ephemeral pycnocline based on:

1. large increase in 5.5 m Ri and 4.5 m $V_{ice}/u_*$ ratio;
2. lack of change in wML N$^2$ despite significant freshwater input from the ice;
3. basal latent heat flux greatly exceeded the 4.5 m and 6.5 m turbulent heat flux estimates;
4. large increases to freshwater storage and $<w'S'>$ after sML development.

The confinement of shear mixing to this shallow fresh layer had important consequences for the development of the NSTM and sML that later occurred in Stage III (refer to Figure 17 process schematic for follow on discussion). Calm winds after the YD 184 mixing event permitted sea ice melt water to collect under the ice-ocean interface forming a near-surface fresh layer and associated ephemeral pycnocline. The primary source of this meltwater into the ephemeral layer is suspected to be melt pond drainage based on the

timing of surface drainage events from webcam and satellite imagery. A particularly large melt pond drainage event is believed to have occurred around YD 189 when warm water began to collect under the sea ice (Figure 8a). When winds increased on YD 192, $u_*$ values increased also as the near-surface active mixing layer deepens past the 4.5 m sensor forming the sML. The large increase in 4.5 m turbulent salt fluxes and sML freshwater storage after YD 192 indicates a substantial amount of freshwater was sequestered above the budget control volume prior to sML development. This freshwater is important for the development and survivability of the sML, since it prevents subsequent wind events from mixing out summer halocline stratification.

For the NSTM, the results from Stage II show there were near equal allocations of radiative input between latent heat losses and wML heat storage gains. For this to occur, stage-averaged radiative input into the ocean would have to be equally partitioned between the IOBL exchanging heat with the ice-ocean interface and the unmixed portion of the wML. Vertical integration of $F_{rad-ocn}$ using an average of the *Frey et al.* [2011] visible light absorption coefficients (K = ~0.2) show that this equal partitioning occurs around 3 m below the sea ice. This is the approximate depth of the 4.5 m sensor and consistent with the weak turbulent fluxes observed at this level. These observations suggest that shoaling of the IOBL and the large areal fraction of melt ponds during Stage II were responsible for the emerging NSTM that appeared on YD 190.

### 5.1.3. Late Summer Influences: Mixing, Wind Stress, and Open Water Fraction

The increase in friction velocity ($u_*$) observed in Stages III and IV indicate turbulent mixing intensified following sML development. These increases in $u_*$ were not a consequence of stronger winds during the last half of time series. Evaluation of $u_*$ and winds during periods when the 4.5 m turbulence package was within the active surface mixing layer ($V_{ice}/u_* < 100$) shows post-sML average $u_*$ was 43% more than pre-sML average $u_*$ (0.0045 and 0.0032 m s$^{-1}$, respectively), although average winds were nearly equal (4.2 and 4.4 m s$^{-1}$). These observations show that turbulent drag between the atmosphere through the ice to the ocean in the presence of the thin sML was higher than that of the thicker wML. We were unable to identify the exact cause of this increased mixing with the observations from this study; however, we hypothesize that the post-sML increase in turbulent mixing was likely due to the concentration of interface transported momentum into a smaller boundary layer volume. For the same wind input, more energy was transferred to the ocean with the sML in place.

The development of the sML was accompanied by an expansion of the open water areas around C2, as evident in the evolution of ice conditions in Figure 3. $A_{OWF}$ expanded from 0.05 to 0.26 between the YDs 191 and 200 SAR image estimates (Figure 6b) and resulted in a 45% increase in stage-averaged ocean radiative fluxes from Stage II to Stage III (31 to 45 W m$^{-2}$, Figure 6d). Even with these increases to radiative input, it is unlikely that thermodynamic processes alone generated the observed 21% decrease in ice coverage in just 9 days. During this same 9 day period, divergent conditions were seen in the local wind stress curl field (Figure 12a). We assessed the relative role of lateral melting and wind-forced divergence by calculating the divergent opening of the ice cover following *Stanton et al.* [2012]. In this method, the difference between triangle areas are divided by the total triangle area to estimate open water fraction ($A_{OWF} = [A(t) - A_o(t)]/A(t)$). We apply this method to two separate cluster array configurations: the triangle area made by C2, C3, and ITP-V 70, and the triangle area made by C2, C4, and ITP-V 70. The results of this calculation show that divergence of the cluster configurations increased open water fraction by as much as 0.11 between YDs 191 and 200 (Figure 12b). This indicates that approximately 50% of the increase in the observed $A_{OWF}$ was due to wind-forced divergence.

These observations are consistent with the numerous atmospheric low pressure systems that transited the Canada Basin in the Climate Forecast System Reanalysis data during Stage III (not shown). MIZ cluster GPS tracks show the random ice motions generated by these systems (Figure 1a), which were preceded and followed by the more typical westward trajectories expected on the south side of the Beaufort Gyre. These observations are also consistent with the seasonal weakening of anti-cyclonic winds and ice motion during summer in the Western Arctic [*Yang*, 2006].

The combination of increased ocean radiative input and enhanced mixing increased basal melt rates by 300% following sML development (~1.5 cm d$^{-1}$ without the YD 211–215 event) when compared to pre-sML development (~0.5 cm d$^{-1}$). Increased stress in the sML also altered the partitioning of ocean absorbed radiative heat to 0.86/0.14, with 191 MJ m$^{-2}$ going toward latent heat losses and only 30 MJ m$^{-2}$ toward OML heat storage gains (Figure 9b). These results indicate the IOBL-OML system was very efficient at converting incoming solar radiation to latent heat loss after the sML developed and likely contributed to the overall ice-ocean feedback within the inner Canada Basin pack ice.

### 5.2. Radiative Parameterizations: Use of Large-Scale Imagery

This work shows that radiative fluxes into the ocean can be reasonably estimated using large-scale areal averages of open water and melt pond fractions derived from satellite imagery. Use of this radiative parameterization demonstrates the significance of through-ice radiative input to the summer heat balance, which for this study came to 94 MJ m$^{-2}$ of heat absorbed in the upper ocean. This suggests that radiative parameterizations that only consider the open-water component underestimate the radiative input by 36% over the summer season. Radiative parameterizations that included open water fraction and sea ice but exclude melt ponds only reduce this error to 23%. Of note, these errors could be higher since heat imbalances observed during high melt pond coverage in Stage II (Figure 9d) suggests through-ice radiative contributions were underestimated by our parameterization. Visible satellite imagery is a valuable tool for determining melt pond coverage and associated radiative input; however, this product is often hampered by cloud contamination, is less available, and has relatively small spatial footprints. Given the importance of melt ponds to the upper ocean heat balance and the limitations inherent to visible satellite imagery, development of accurate melt pond fractions from SAR imagery is essential.

### 6. Summary and Conclusions

We have examined the summer evolution of the ice-ocean boundary layer and ocean mixed layer (IOBL-OML) system in the Canada Basin seasonal ice zone. The development of melt ponds in early summer (Stage II) marks the start of significant changes to the dynamic and thermodynamic structure of the upper ocean. Dynamically, stronger near-surface stratification limits the vertical extent of the ice-ocean boundary layer. Through evaluation of freshwater budgets, we find that the buoyancy source for this increased stratification is greater than that supplied by basal melting alone. The additional buoyancy required is likely due to the drainage of melt ponds. In this IOBL-OML regime, radiative input, primarily from transmittance of sunlight through melt ponds, is evenly distributed between the shallow active mixing layer and heat storage in the residual winter mixed layer. Increases to winter mixed layer heat storage during this period accounted for over 50% of the total summer heat input and is the primary source of heat to the developing near-surface temperature maximum.

A near-surface fresh layer and associated ephemeral pycnocline develop under the sea ice during periods of calm winds and melt pond drainage. We infer that meltwater accumulates above this ephemeral pycnocline until wind forcing deepens the layer through shear-driven turbulent processes to form the summer mixed layer (Stage III). We find that the amount of freshwater sequestered in this shallow active mixing layer is critical for the development and survivability of the summer mixed layer to prevent subsequent wind events from mixing out summer halocline stratification.

The partitioning of radiative heat input within the IOBL-OML system changes following development of the summer mixed layer. Stronger turbulent mixing leads to larger ocean-to-ice heat fluxes and higher basal melt rates. In this study, radiative input was redistributed 0.86/0.14 between latent heat losses and ocean mixed layer heat storage after the summer mixed layer developed. Concurrent with these changes in the IOBL-OML system, wind-forced divergence in the sea ice marked an important transition in radiative input as larger open water areas allowed more radiative fluxes into the ocean. This occurred despite the lower solar irradiance in late summer and decrease in melt pond coverage.

During the marginal ice zone portion of the drift (Stage IV), continued expansion of open water areas further increased ocean radiative forcing. We estimated that solar input to the ocean during this period accounted for almost half of the total summer radiative input. Basal melt rates were high and variability was large. A single 4 day event, during which turbulent heat fluxes attained values as high as 200 W m$^{-2}$, accounted for ~20% of the total summer basal melt. Weak circuitous motion of the sea ice, driven by midsummer atmospheric conditions, allows differential heating of the under-ice and open-water summer mixed layers. These spatially heterogeneous conditions can lead to patches of enhanced melting on the underside of the ice cover, well away from the Canada Basin seasonal ice zone ice edge. During stronger more persistent forcing, typical under an established Beaufort High, the upper ocean is well mixed horizontally and basal melting is expected to be more uniform.

Overall, these results suggest that the early summer upper ocean evolution is closely linked to the evolution of melt ponds on the sea ice surface. In late summer, the influence of melt ponds reduces and the upper ocean evolution is driven primarily by the increase in turbulent mixing in the summer mixed layer and the fraction of open water in the marginal ice zone.

Regional comparisons conducted across the Canada Basin show that the upper ocean evolution described above was similar across much of the Basin. Heat and freshwater storage gains in early summer were nearly identical in timing and magnitude. The subsequent development of the summer mixed layer and NSTM occurred on nearly the same day throughout the seasonal ice zone. In late summer, properties of the upper ocean are more dependent on seasonal ice zone location, with differences attributed to variations in the open water fraction across the extensive Canada Basin marginal ice zone. These results suggest that the dominant processes driving the thermodynamics of the Canada Basin seasonal ice zone are regional in scale prior to marginal ice zone development, with more localize influences afterward.

1-D local mixed layer heat budgets closed reasonably well, with solar radiative input (source) accounting for at least 89% of the latent heat losses (sink #1) and heat storage gains (sink #2) observed at cluster 2 (sink terms partitioned 0.77/0.23, respectively). These results suggest that the seasonal ice zone system receives enough local radiative input into the upper ocean to achieve the observed late summer conditions, without substantial advective contributions from the ice edge. We term this inside-out method of ice melt the "thermodynamically forced marginal ice zone," which stands in contrast to the outside-in development typical of an Eastern Arctic marginal ice zone where thinning sea ice diminishes under a combination of mechanical and thermodynamic edge effects. This could explain the large area of deteriorating sea ice observed in the Canada Basin seasonal ice zone away from the sea ice edge during the 2014 summer season (Figure 1b).

## References

Cole, S. T., M.-L. Timmermans, J. M. Toole, R. A. Krishfield, and F. T. Thwaites (2014), Ekman veering, internal waves, and turbulence observed under Arctic Sea Ice, *J. Phys. Oceanogr.*, *44*(5), 1306–1328, doi:10.1175/JPO-D-12-0191.1.

Cole, S. T., F. T. Thwaites, R. A. Krishfield, and J. M. Toole (2015), Processing of velocity observations from Ice-Tethered Profilers, in *IEEE OCEANS 2015 Conference Publications-MTS/IEEE Washington*, IEEE, pp. 1–10, Washington, D. C.

Eicken, H., H. R. Krouse, D. Kadko, and D. K. Perovich (2002), Tracer studies of pathways and rates of meltwater transport through Arctic summer sea ice, *J. Geophys. Res.*, *107*(C10), 8046, doi:10.1029/2000JC000583.

Frey, K. E., D. K. Perovich, and B. Light (2011), The spatial distribution of solar radiation under a melting Arctic sea ice cover, *Geophys. Res. Lett.*, *38*, L22501, doi:10.1029/2011GL049421.

Hayes, D. R., and J. Morison (2008), Ice-ocean turbulent exchange in the Arctic summer measured by an autonomous underwater vehicle, *Limnol. Oceanogr.*, *53*(5_part_2), 2287–2308, doi:10.4319/lo.2008.53.5_part_2.2287.

Hsu, S. A., E. A. Meindl, and D. D. Gilhousen (1994), Determining the power-law wind profile exponent under near-neutral stability conditions at sea, *J. Appl. Meteorol.*, *33*, 757–765, doi:10.1175/1520-0450(1994)033 < 0757:DTPLWP>2.0.CO;2.

Jackson, J. M., E. C. Carmack, F. A. McLaughlin, S. E. Allen, and R. G. Ingram (2010), Identification, characterization, and change of the near-surface temperature maximum in the Canada Basin, 1993–2008, *J. Geophys. Res.*, *115*, C05021, doi:10.1029/2009JC005265.

Jackson, J. M., S. E. Allen, F. A. McLaughlin, R. A. Woodgate, and E. C. Carmack (2011), Changes to the near-surface waters in the Canada Basin, Arctic Ocean from 1993–2009, *J. Geophys. Res.*, *116*, C10008, doi:10.1029/2011JC007069.

Jackson, J. M., W. J. Williams, and E. C. Carmack (2012), Winter sea-ice melt in the Canada Basin, Arctic Ocean, *Geophys. Res. Lett.*, *39*, L03603, doi:10.1029/2011GL050219.

Jackson, K., J. Wilkinson, T. Maksym, D. Meldrum, J. Beckers, C. Haas, and D. Mackenzie (2013), A novel and low-cost sea ice mass balance buoy, *J. Atmos. Oceanic Technol.*, *30*(11), 2676–2688, doi:10.1175/JTECH-D-13-00058.1.

Kim, T. S., K. A. Park, M. S. Lee, J. J. Park, S. Hong, K. L. Kim, and E. Chang (2013), Application of bimodal histogram method to oil spill detection from a satellite synthetic aperture radar image, *Korean J. Remote Sens.*, *29*(6), 645–655, doi:10.7780/kjrs.2013.29.6.7.

Krishfield, R., J. Toole, A. Proshutinsky, and M.-L. Timmermans (2008), Automated ice-tethered profilers for seawater observations under pack ice in all seasons, *J. Atmos. Oceanic Technol.*, *25*(11), 2091–2105, doi:10.1175/2008JTECHO587.1.

Lane, L. S. (1997), Canada Basin, Arctic Ocean: Evidence against a rotational origin, *Tectonics*, *16*(3), 363–387, doi:10.1029/97TC00342.

Large, W. G., J. C. McWilliams, and S. C. Doney (1994), Oceanic vertical mixing: A review and a model with a nonlocal boundary layer parameterization, *Rev. Geophys.*, *32*(4), 363–403, doi:10.1029/94RG01872.

Lee, C. M., et al. (2012), Marginal Ice Zone (MIZ) program: Science and experiment plan, *Tech. Rep. APL-UW 1201*, 48 pp., Appl. Phys. Lab., Univ. of Wash., Seattle, Wash.

Light, B. T., T. C. Grenfell, and D. K. Perovich (2008), Transmission and absorption of solar radiation by Arctic sea ice during the melt season, *J. Geophys. Res.*, *113*, C03023, doi:10.1029/2006JC003977.

Macdonald, R. W., E. C. Carmack, F. A. McLaughlin, K. K. Falkner, and J. H. Swift (1999), Connections among ice, runoff and atmospheric forcing in the Beaufort Gyre, *Geophys. Res. Lett.*, *26*(15), 2223–2226, doi:10.1029/1999GL900508.

McPhee, M. G. (1992), Turbulent heat flux in the upper ocean under sea ice, *J. Geophys. Res.*, *97*(C4), 5365, doi:10.1029/92JC00239.

McPhee, M. G. (2008), *Air-Ice-Ocean Interaction: Turbulent Ocean Boundary Layer Exchange Processes*, 215 pp., Springer, Dordrecht, Netherlands.

McPhee, M. G., G. A. Maykut, and J. H. Morison (1987), Dynamics and thermodynamics of the ice/upper ocean system in the marginal ice zone of the Greenland Sea, *J. Geophys. Res.*, *92*(C7), 7017, doi:10.1029/JC092iC07p07017.

MIZEX Group (1986), MIZEX East 83/84: The summer marginal ice zone program in the Fram Strait/Greenland Sea, *Eos Trans. AGU*, *67*(23), 513–517, doi:10.1029/EO067i023p00513.

Morison, J. H., M. G. McPhee, and G. A. Maykut (1987), Boundary layer, upper ocean, and ice observations in the Greenland Sea marginal ice zone, *J. Geophys. Res.*, *92*(C7), 6987–7011, doi:10.1029/JC092iC07p06987.

Nghiem, S. V., D. K. Hall, I. G. Rigor, P. Li, and G. Neumann (2014), Effects of Mackenzie River discharge and bathymetry on sea ice in the Beaufort Sea, *Geophys. Res. Lett.*, *41*, 873–879, doi:10.1002/2013GL058956.

Paulson, C. A., and W. S. Pegau (2001), The summertime thermohaline evolution of an Arctic lead: Heat budget of the surface layer, in *Proceedings of the Sixth Conference on Polar Meteorology and Oceanography*, pp. 271–274, Am. Meteorol. Soc., San Diego, Calif.

Pegau, W. S., and C. A. Paulson (2001), The albedo of Arctic leads in summer, *Ann. Glaciol.*, *33*, 221–224, doi:10.3189/172756401781818833.

Perovich, D. K., and C. Polashenski (2012), Albedo evolution of seasonal Arctic sea ice, *Geophys. Res. Lett.*, *39*, L08501, doi:10.1029/2012GL051432.

Perovich, D. K., T. C. Grenfell, B. Light, and P. V. Hobbs (2002), Seasonal evolution of the albedo of multiyear Arctic sea ice, *J. Geophys. Res.*, *107*(C10), 8044, doi:10.1029/2000JC000438.

Perovich, D. K., B. Light, H. Eicken, K. F. Jones, K. Runciman, and S. V. Nghiem (2007a), Increasing solar heating of the Arctic Ocean and adjacent seas, 1979–2005: Attribution and role in the ice-albedo feedback, *Geophys. Res. Lett.*, *34*, L19505, doi:10.1029/2007GL031480.

Perovich, D. K., S. V. Nghiem, T. Markus, and A. Schweiger (2007b), Seasonal evolution and interannual variability of the local solar energy absorbed by the Arctic sea ice-ocean system, *J. Geophys. Res.*, *112*, C03005, doi:10.1029/2006JC003558.

Perovich, D. K., W. Meier, J. Maslanik, and J. Richter-Menge (2012), Sea ice cover [in State of the Climate in 2011], *Bull. Am. Meteorol. Soc.*, *3*(7), S140–S142.

Persson, P. O. G., C. W. Fairall, E. L. Andreas, P. S. Guest, and D. K. Perovich (2002), Measurements near the Atmospheric Surface Flux Group tower at SHEBA: Near-surface conditions and surface energy budget, *J. Geophys. Res.*, *107*(C10), 8045, doi:10.1029/2000JC000705.

Polashenski, C., D. Perovich, J. Richter-Menge, and B. Elder (2011), Seasonal ice mass-balance buoys: Adapting tools to the changing Arctic, *Ann. Glaciol.*, *52*(57), 18–26. doi:10.3189/172756411795931516.

Polashenski, C., D. Perovich, and Z. Courville (2012), The mechanisms of sea ice melt pond formation and evolution, *J. Geophys. Res.*, *117*, C01001, doi:10.1029/2011JC007231.

Price, J. F., R. A. Weller, and R. Pinkel (1986), Diurnal cycling: Observations and models of the upper ocean response to diurnal heating, cooling, and wind mixing, *J. Geophys. Res.*, *91*(C7), 8411–8427, doi:10.1029/JC091iC07p08411.

Proshutinsky, A., R. Krishfield, M.-L. Timmermans, J. Toole, E. Carmack, F. McLaughlin, W. J. Williams, S. Zimmermann, M. Itoh, and K. Shimada (2009), Beaufort Gyre freshwater reservoir: State and variability from observations, *J. Geophys. Res.*, *114*, C00A10, doi:10.1029/2008JC005104.

Saha, S., et al. (2010), The NCEP climate forecast system reanalysis, *Bull. Am. Meteorol. Soc.*, *91*, 1015–1057, doi:10.1175/2010BAMS3001.1.

Salah, M. B., A. Mitiche, and I. B. Ayed (2011), Multiregion image segmentation by parametric Kernel graph cuts, *IEEE Trans. Image Process.*, *20*(2), 545–557, doi:10.1109/TIP.2010.2066982.

Shaw, W. J., and J. H. Trowbridge (2001), The direct estimation of near-bottom turbulent fluxes in the pressence of energetic wave motions, *J. Atmos. Oceanic Technol.*, *18*(9), 1540–1557, doi:10.1175/1520-0426(2001)018 $<$ 1540:TDEONB$>$2.0.CO;2.

Shaw, W. J., T. P. Stanton, M. G. McPhee, J. H. Morison, and D. G. Martinson (2009), Role of the upper ocean in the energy budget of Arctic sea ice during SHEBA, *J. Geophys. Res.*, *114*, C06012, doi:10.1029/2008JC004991.

Stanton, T. P., W. J. Shaw, and J. K. Hutchings (2012), Observational study of relationships between incoming radiation, open water fraction, and ocean-to-ice heat flux in the Transpolar Drift: 2002–2010, *J. Geophys. Res.*, *117*, C07005, doi:10.1029/2011JC007871.

Steele, M., J. Zhang, and W. Ermold (2010), Mechanisms of summertime upper Arctic Ocean warming and the effect on sea ice melt, *J. Geophys. Res.*, *115*, C11004, doi:10.1029/2009JC005849.

Stegall, S. T., and J. Zhang (2012), Wind field climatology, changes, and extremes in the Chukchi-Beaufort Seas and Alaska North Slope during 1979–2009, *J. Clim.*, *25*, 8075–8089, doi:10.1175/JCLI-D-11-00532.1.

Thomson, J., and E. Rogers (2014), Swell and sea in the emerging Arctic Ocean, *Geophys. Res. Lett.*, *41*, 3136–3140, doi:10.1002/2014GL059983.

Timmermans, M.-L. (2015), The impact of stored solar heat on Arctic sea ice growth, *Geophys. Res. Lett.*, *42*, 6399–6406, doi:10.1002/2015GL064541.

Timmermans, M.-L., A. Proshutinsky, E. Golubeva, J. M. Jackson, R. Krishfield, M. McCall, G. Platov, J. Toole, W. Williams, T. Kikuchi, and S. Nishino (2014), Mechanisms of Pacific Summer Water variability in the Arctic's Central Canada Basin, *J. Geophys. Res. Oceans*, *119*, 7523–7548, doi:10.1002/2014JC010273.

Tivy, A., S. E. L. Howell, B. Alt, S. McCourt, R. Chagnon, G. Crocker, T. Carrieres, and J. J. Yackel (2011), Trends and variability in summer sea ice cover in the Canadian Arctic based on the Canadian Ice Service Digital Archive, 1960–2008 and 1968–2008, *J. Geophys. Res.*, *116*, C03007, doi:10.1029/2009JC005855.

Tomasi, C., and R. Manduchi (1998), Bilateral filtering for gray and color images, in *Proceedings of the 1998 IEEE International Conference on Computer Vision*, IEEE, pp. 839–846, Bombay, India, doi:10.1109/ICCV.1998.710815.

Toole, J. M., M.-L. Timmermans, D. K. Perovich, R. A. Krishfield, A. Proshutinsky, and J. A. Richter-Menge (2010), Influences of the ocean surface mixed layer and thermohaline stratification on Arctic Sea ice in the central Canada Basin, *J. Geophys. Res.*, *115*, C10018, doi:10.1029/2009JC005660.

Toole, J. M., R. A. Krishfield, M.-L. Timmermans, and A. Proshutinsky (2011), The Ice-Tethered Profiler: ARGO of the Arctic, *Oceanography*, *24*(3), 162–173, doi:10.5670/oceanog.2011.65.

UNESCO (1983), *UNESCO Joint Panel on Oceanographic Tables and Standards: Algorithms for Computation of Fundamental Properties of Seawater*, UNESCO Techinal Papers in Marine Science, vol. 44, 53 pp., UNESCO, Paris.

Vivier, F., J. K. Hutchings, Y. Kawaguchi, T. Kikuchi, J. H. Morison, A. Lourenco, and T. Noguchi (2016), Sea ice melt onset associated with lead opening during the spring/summer transition near the North Pole, *J. Geophys. Res. Oceans*, *121*, 2499–2522, doi:10.1002/2015JC011588.

Wadhams, P. (2000), *Ice in the Ocean*, 364 pp., Gordon and Breach, Amsterdam, Netherlands.

Yang, J. (2006), The seasonal variability of the Arctic Ocean Ekman transport and its role in the mixed layer heat and salt fluxes, *J. Clim.*, *19*(20), 5366–5387, doi:10.1175/JCLI3892.1.

Zhang, J., R. Lindsay, and A. Schweiger (2013), The impact of an intense summer cyclone on 2012 Arctic sea ice retreat, *Geophys. Res. Lett.*, *40*, 720–726, doi:10.1002/grl.50190.